

Identifying Surface Degeneracies in Single-Visit Reflected Light Observations of Modern Earth using the Habitable Worlds Observatory

AIDEN S. ZELAKIEWICZ ^{1,2,*} ELIJAH MULLENS ^{1,2} LISA KALTENEGER ^{1,2} AND DMITRY SAVRANSKY ^{1,2,3}

¹*Department of Astronomy, Cornell University, 122 Sciences Drive, Ithaca, NY 14853, USA*

²*Carl Sagan Institute, Cornell University, 311 Space Sciences Building, Ithaca, NY 14853, USA*

³*Sibley School of Mechanical and Aerospace Engineering, Cornell University, Ithaca, NY 14853, USA*

ABSTRACT

Characterizing the surface and atmosphere of Earth-like planets in reflected light is a key goal for upcoming direct imaging surveys. NASA’s next flagship-class astrophysics mission concept, the Habitable Worlds Observatory (HWO), is a space-based Ultraviolet/Optical/Near-Infrared observatory with a mission design requirement to reach the 10^{-10} contrast necessary to characterize Earth-like planets around Sun-like stars. While reflected light from planetary surfaces provides a unique opportunity to constrain the coverage of surface materials and biopigments, detailed predictions of HWO’s ability to retrieve surface fractions are necessary but have not been conducted. Here, we model photon-counting noise from astrophysical, instrumental, and post-processing sources for the HWO Exploratory Analytic Case 5 design equipped with a charge-6 vector-vortex coronagraph. By combining our photon-counting noise with five distinct modern Earth models at quadrature, we simulate single-visit HWO observations and perform spectral retrievals using the open-source code POSEIDON to assess our ability to constrain both the surface and atmospheric composition. We find that degeneracies between planetary radius, surface pressure, surface material, and cloud coverage in reflected-light retrievals can significantly complicate the classification of surface features. These degeneracies can complicate the detection of surface biopigments, such as the chlorophyll-induced red edge on modern Earth. Our work shows that developing concrete strategies for detecting surface features and breaking degeneracies in reflected-light observations of Earth-like planets is a critical priority for mission design and data analysis.

1. INTRODUCTION

With over 6,000 exoplanets confirmed to date (J. L. Christiansen et al. 2025), and tens of thousands more predicted to be found with upcoming observatories like the *Nancy Grace Roman Space Telescope* (R. F. Wilson et al. 2023) and *PLATO* (H. Rauer et al. 2025), the field of exoplanet science has entered an era of characterization and demographic studies. Atmospheric characterization using the *James Webb Space Telescope* (*JWST*) is unveiling features such as molecular abundances (T. J. Bell et al. 2023; B. Benneke et al. 2024; T. G. Beatty et al. 2024; S. P. Schmidt et al. 2025), aerosols (D. Grant et al. 2023; A. Dyrek et al. 2024; J. Inglis et al. 2024), and photochemistry (S.-M. Tsai et al. 2023; Z. Rustamkulov et al. 2023) in transiting hot Jupiters and sub-Neptunes. Transmission and emission spectroscopy of Earth-like planets, however, is significantly more difficult due to factors such as the shallower transit depth (L. Kaltenegger & W. A. Traub 2009). Despite the chal-

lenges, *JWST* observations of rocky exoplanets orbiting M-dwarfs have begun to place upper limits on secondary atmospheres (Q. Xue et al. 2024; M. Radica et al. 2025; M. Fortune et al. 2025; K. A. Bennett et al. 2025; N. Espinoza et al. 2025; A. Glidden et al. 2025). While M-dwarfs improve the observability of rocky exoplanets compared to Sun-like stars, their increased activity, especially young M-dwarfs, may expose close-in planets to atmospheric stripping due to high-energy irradiation. Stellar activity may also present signals larger than attenuation from the planet itself, which require an in-depth understanding of the star to address (J. Scalo et al. 2007; H. Lammer et al. 2007; P. J. Wheatley et al. 2017; L. Kaltenegger 2017; K. J. Zahnle & D. C. Catling 2017).

The 2020 Decadal Survey on Astronomy and Astrophysics by the National Academies of Science, Engineering, and Medicine identified imaging Earth-like planets around Sun-like stars as a top priority for the field (E. National Academies of Sciences 2021). Following the recommendations of the 2020 Decadal Survey, NASA announced the Habitable Worlds Observatory (HWO)

* New York Space Grant Fellow

as the next flagship-class astrophysics mission design concept, taking inspiration from the LUVOIR (The LUVOIR Team 2019) and HabEx (B. S. Gaudi et al. 2020) concepts. The HWO design is a ≥ 6 meter space-based observatory with a dedicated survey for the detection and characterization of Earth-like exoplanets around FGK stars (N. W. Tuchow et al. 2025; S. Peacock et al. 2025). A driving science goal of HWO is to characterize exoplanets around FGK stars, with particular emphasis on Earth-like planets around Sun-like stars. To observe an Earth-twin orbiting a Sun-analog, HWO will need to reach a planet-star flux ratio (F_p/F_s) below 10^{-10} through high-contrast imaging.

As part of the Great Observatory Maturation Program (GOMAP), the Technology Assessment Group (TAG) has been leading the design of Exploratory Analytic Cases (EACs) for HWO (E. National Academies of Sciences 2021; L. Feinberg et al. 2024). The EACs were created to model and inform key mission design choices as the Concept Maturity Level timeline for HWO progresses. The first three EAC design efforts, which ranged from 6 to 8 meters, were completed in 2025, with EACs 4 and 5 currently being assessed by the TAG. The EAC 4 and 5 primary mirrors have an inscribed diameter of > 6.5 and > 8 meters, respectively (L. D. Feinberg et al. 2026). Both observatory designs feature hexagonal segmented primary mirrors and an off-axis secondary. The EACs are compatible with a coronagraph instrument (CI), which will enable visible (VIS) and near-infrared (NIR) spectroscopy using an integral field spectrograph (IFS) to capture reflected light from an Earth-sized exoplanet.

In the wavelength regime of HWO, reflected light from the host star is expected to be the primary component of emergent flux from the planet. Reflection spectroscopy of Earth-like exoplanets has the potential to uncover biosignatures unique to surface features, such as biopigments, including the chlorophyll-induced photosynthetic red edge at ~ 750 nm (C. Sagan et al. 1993; S. Seager et al. 2005; L. Kaltenegger 2017). Ongoing research on identifying potential atmospheric biosignatures on other worlds (see L. Kaltenegger 2017; E. W. Schwieterman et al. 2018; E. W. Schwieterman & M. Leung 2024, for reviews), and biopigments on Earth (S. Hegde & L. Kaltenegger 2013; S. Hegde et al. 2015; J. T. O’Malley-James & L. Kaltenegger 2018a, 2019; L. F. Coelho et al. 2022, 2024; L. F. Coelho et al. 2025) have shown the incredible spectral diversity of life. Detecting surface biopigments on terrestrial exoplanets will require rigorous protocols for signal detection and vetting (V. Meadows et al. 2022).

Here, we examine whether current state-of-the-art methods for analyzing exoplanet atmospheres via Bayesian atmospheric retrievals (see N. Madhusudhan 2018; J. K. Barstow & K. Heng 2020; R. J. MacDonald & N. E. Batalha 2023, for reviews) can identify surface features in addition to atmospheric features. Retrieval codes are the standard for analyzing *JWST* transmission and emission spectra, and many of these algorithms are now being developed to handle higher-resolution reflection spectra for next-generation observatories. These codes must account for the unique spectral signatures of surface pigmentation from both abiotic and biotic sources, as well as for attenuation by atmospheric gases and aerosols.

Work has begun on constructing frameworks to determine the surface composition of exoplanet reflection spectra. The simplest and most agnostic surface treatment is to assume a constant, wavelength-independent surface albedo (Y. K. Feng et al. 2018; M. Damiano & R. Hu 2022; A. Salvador & T. D. Robinson 2025). Assuming a constant surface albedo reduces computational cost and model complexity, but it does not capture the unique spectral characteristics of individual surface components (J. Madden & L. Kaltenegger 2020a). To capture the wavelength dependence of surface reflectivity while remaining agnostic to prior information about the planet, some studies have developed schemes to analytically reproduce the planet’s surface albedo, successfully placing constraints on Earth’s photosynthetic red edge (F. Wang et al. 2022; J. Gomez Barrientos et al. 2023; Z. Burr et al. 2026) and the overall structure of Earth’s surface albedo (A. G. Ulses et al. 2025). However, while implementing analytical treatments of the albedo profile is ideal for capturing wavelength dependence, it can increase the dimensionality of the retrieval as more complex structures are sought to be captured, thereby substantially increasing computational time.

To determine the specific composition of the planetary surface, laboratory-measured wavelength-dependent albedo data are necessary in the retrieval process. Retrievals on a lifeless Earth (A. G. Ulses et al. 2025) placed constraints on surface coverage using ultraviolet (UV), VIS, and NIR data. A. G. Ulses et al. (2025) found that including UV observations down to $0.3 \mu\text{m}$ is necessary to break degeneracies between O_3 abundance, planet size, and surface properties. However, this analysis used the same set of input spectra in the forward model as in the retrieval, and the choice of laboratory data sources can significantly bias surface spectra (G. Roccetti et al. 2024, 2025). Thorough tests of the method’s effectiveness using spectra from commonly used databases on unknown surface compositions

are critical for assessing its validity, yet have not been done.

Here, we perform surface and atmospheric retrievals on simulated single-visit observations of a modern Earth twin to identify degeneracies in reflected-light retrievals of Earth-like exoplanets. We chose to focus on the largest EAC design concept, a 10-meter (8.3 meter inscribed diameter) EAC 5, to simulate HWO observations of five distinct modern Earth spectral models. In Section 2, we outline our methodology for modeling the modern Earth spectra, our HWO noise model, and discuss the retrieval algorithm and initialization. We explore the retrieval results for each of the five spectra models in Section 3. In Section 4, we summarize the results in the context of current retrieval algorithms and recommendations for future work.

2. METHODS

To constrain the surface and atmosphere of Earth-like exoplanets, we use the open-source exoplanet retrieval code POSEIDON (R. J. MacDonald & N. Madhusudhan 2017; R. J. MacDonald 2023),¹ that can perform retrievals for transmission, emission (L.-P. Coulombe et al. 2023), and reflection spectroscopy (E. Mullens et al. 2024). The reflection capabilities in POSEIDON were adapted from PICASO (N. E. Batalha et al. 2019) and originally described in the POSEIDON v1.2 release (E. Mullens et al. 2024). Here, we use an updated forward model prescription to include wavelength-dependent surfaces using lab-derived albedos (E. Mullens et al. 2026, Submitted). For a complete description of the radiative transfer and the module rework that enables HWO-specific analyses, see E. Mullens et al. (2026, Submitted).

Modern Earth serves as an ideal testbed for this analysis, owing to the extensive work undertaken to characterize Earth and the goal of detecting Earth twins beyond the Solar System (C. Sagan et al. 1993; L. Kaltenegger et al. 2007; T. D. Robinson et al. 2011; S. Rugheimer et al. 2013; Y. K. Feng et al. 2018; L. Kaltenegger et al. 2020b; K. E. Goodis Gordon et al. 2024). We perform exoplanet retrievals on five synthetic forward-modeled modern Earth spectra, which can be categorized into two groups: three spectra using only POSEIDON’s forward modeling capabilities, and two spectra based on complex atmospheric and surface models of modern Earth. The first three spectra are generated entirely within POSEIDON and share identical parametric descriptions of the atmospheric gas-phase, temperature, and surface properties, with the goal of varying cloud cover. These

three spectra also use the same parametric description as the retrieval algorithm, as discussed in Sec. 2.5, thereby enabling testing of the retrieval algorithm’s performance under varying cloud coverages. The fourth model combines a complex atmospheric pressure-temperature (P-T) and chemical mixing profile from EXO-Prime (L. Kaltenegger et al. 2020a) with an in-depth surface prescription derived from observations with the Moderate Resolution Imaging Spectrometer (MODIS) (V. V. Salomonson et al. 1989). The radiative transfer for this fourth spectrum is computed within POSEIDON, but using the more complex atmosphere and surface models. We source the fifth spectrum from G. Rocchetti et al. (2025), which combines the 3D radiative-transfer code MYSTIC (B. Mayer 2009; B. Mayer et al. 2010) with surface spectra from the HAMSTER (G. Rocchetti et al. 2024) hyperspectral albedo dataset.

We define the bulk planetary properties of our terrestrial planet to have surface radius $R_p = R_\oplus$, mass $M_p = M_\oplus$, and orbital distance $r_p = 1$ AU. The Earth twin orbits a G2V star with solar metallicity ($[\text{Fe}/\text{H}] = 0$), solar $\log_{10} g = 4.4$, and effective temperature $T_{\text{eff}} = 5772$ K, where g is the solar surface gravity in cm/s^2 . In accordance with mission goals for HWO (E. National Academies of Sciences 2021) and current potential target stars (E. Mamajek & K. Stapelfeldt 2024; N. W. Tychow et al. 2025; S. Peacock et al. 2025), we assume the system is observed at a distance of 10 pc.

Reflected light observations for a planet are expressed as the planet-star flux ratio

$$\frac{F_{p,\lambda}}{F_{s,\lambda}} = A_g(\lambda)\Phi(\alpha)\left(\frac{R_p}{r_p}\right)^2, \quad (1)$$

where $\Phi(\alpha)$ is the planetary orbital phase function and $A_g(\lambda)$ is the geometric albedo. The orbital phase angle α is defined as the angle at the planet between the star and observer (i.e., the star-planet-observer angle). T. D. Robinson (2025), through what they called a “happy accident,” discovered that a normalized Henyey-Greenstein (HG) phase function (L. G. Henyey & J. L. Greenstein 1941)

$$\Phi(\alpha, \bar{g})_{\text{HG}} = \frac{P_{\text{HG}}(\alpha, \bar{g})}{P_{\text{HG}}(\alpha = 0^\circ, \bar{g})}, \quad (2)$$

with asymmetry parameter $\bar{g} = -1/3$ closely reproduces Earth’s phase curve. The HG phase function at a given phase angle and asymmetry parameter is given by

$$P_{\text{HG}}(\alpha, \bar{g}) = \frac{1 - \bar{g}^2}{[1 + \bar{g}^2 - 2\bar{g}\cos(\pi - \alpha)]^{3/2}}, \quad (3)$$

¹ <https://github.com/MartianColonist/POSEIDON>

where the scattering angle $\Theta = \pi - \alpha$. The optimal α to maximize F_p/F_s occurs at the root of

$$2 \cos(\alpha)\Phi(\alpha) + \sin(\alpha)\frac{\partial\Phi(\alpha)}{\partial\alpha} = 0, \quad (4)$$

for any choice of $\Phi(\alpha)$ (R. A. Brown 2004). For the normalized HG phase function at $\bar{g} = -1/3$, we find that $\alpha_{\max} = 60^\circ.97$ maximizes the planet-star flux ratio. Generalizing to any asymmetry parameter in the range $\bar{g} = (-1, 1)$, we find the result that the optimal phase angle for $\Phi(\alpha, \bar{g})_{\text{HG}}$ can be approximately fit by a straight line with $\alpha_{\max} \approx 90^\circ(1 + \bar{g})$.

Since the reflection spectra we produce with POSEIDON and acquired from G. Rocchetti et al. (2025) are at full phase ($\alpha = 0^\circ$), we apply Eqn. 2 to simulate observations with HWO. We assume the Earth-like exoplanet is observed at quadrature ($\alpha = 90^\circ$) and adopt $\bar{g} = -1/3$ from T. D. Robinson (2025) to produce Earth’s phase curve analytically. When we perform retrievals on HWO datasets, we cannot assume knowledge of the planet’s phase function. Coarse constraints on α may be possible from orbital fitting on photometric observations prior to deep spectroscopic characterization. During retrievals, we scale the spectra (and their associated errors) back to full phase for computational purposes only.

2.1. POSEIDON Consistent Spectra

We first test the retrieval capabilities of POSEIDON on HWO-quality synthetic datasets generated from three forward-model spectra created within POSEIDON. These forward models are constructed from the parametric descriptions available in POSEIDON’s forward-modeling and retrieval modules, enabling an *apples-to-apples* comparison of HWO synthetic data with varying cloud coverage. We create a parametric $T = 300$ K isothermal atmosphere with H_2O , O_2 , and N_2 opacity sources from HITRAN (I. E. Gordon et al. 2017; I. E. Gordon et al. 2022) in addition to O_3 from A. Serdyuchenko et al. (2014) via POSEIDON’s temperate opacity database (Z. Lin et al. 2021). We assign uniform vertical mixing ratios of $\log_{10}(\text{H}_2\text{O}) = -3$, $\log_{10}(\text{O}_3) = -6$, and $\log_{10}(\text{O}_2) = -0.7$, where the remainder of the atmosphere is filled with N_2 . $\text{N}_2\text{-N}_2$, $\text{N}_2\text{-H}_2\text{O}$, $\text{O}_2\text{-O}_2$, and $\text{O}_2\text{-N}_2$ collision-induced absorption (CIA) opacity sources from HITRAN (T. Karman et al. 2019) are also included. The atmosphere is constructed using a 200-layer pressure grid ranging from 10^2 to 10^{-6} bar with logarithmic spacing, with the opaque reflecting surface set at 1 bar. Unlike many pressure grids used in spectral models, which assume a constant logarithmic scale, we adopt a custom pressure grid. Between 10^{-6} and 10^{-2} bar, we place 50 pressure layers and 150 pressure layers

Table 1. Summary of parameters used to model the three self-consistent POSEIDON Earth-like exoplanet spectra and retrievals.

Variable	Unit	Input	Retrieval Prior
Star			
T_{eff}	K	5772	—
$\log_{10} g$	cm/s ²	4.4	—
[Fe/H]	dex	0	—
Planet			
R_p	R_{\oplus}	1	$\mathcal{U}(0.1, 10)$
$\log_{10} P_{\text{surf}}$	bar	0	$\mathcal{U}(-3, 2)$
T	K	300	$\mathcal{U}(100, 400)$
α	degree	90	—
r_p	AU	1	—
Mixing Ratios			
$\log_{10} \text{H}_2\text{O}$	—	-3	$\mathcal{U}(-12, 0)$
$\log_{10} \text{O}_3$	—	-6	$\mathcal{U}(-12, 0)$
$\log_{10} \text{O}_2$	—	-0.7	$\mathcal{U}(-12, 0)$
H₂O Clouds			
f_{cloud}	—	(0, 0.5, 1)	$\mathcal{U}(0, 1)$
$\log_{10} P_{\text{top}}$	bar	$\log_{10}(0.5)$	$\mathcal{U}(-4, 0)$
$\Delta \log_{10} P$	bar	$\log_{10}(1.2)$	$\mathcal{U}(0.1, 3)$
$\log_{10} r_m$	μm	0	$\mathcal{U}(-1, 1)$
$\log_{10} \text{H}_2\text{O}$	—	-3	$\mathcal{U}(-8, 0)$
Surface			
f_{forest}	—	0.15	$\mathcal{U}(0, 1)$
f_{ocean}	—	0.7	$\mathcal{U}(0, 1)$
f_{snow}	—	0.05	$\mathcal{U}(0, 1)$
f_{sand}	—	0.1	$\mathcal{U}(0, 1)$

between 10^{-2} and 10^2 bar. The higher resolution of the pressure grid from 10^{-2} to 10^2 bar allows us to resolve detailed structures in the troposphere and lower stratosphere, such as clouds, which can be thin in pressure space. We prescribe the opaque surface as 70% ocean, 15% forest, 5% snow and ice, and 10% sand, represented by the Ocean, Aspen, Antarctic, and Sand spectra listed in Table 2. In panel (B) of Fig. 1, the red curve in the top panel is the weighted surface spectra used in the forward model, and the individual components are shown in the bottom panel.

Table 2. Surface spectra used in this study, as well as their percent surface coverage in the MODIS-derived surface spectra.

Surface Name	Coverage (%)	Reference	Spectrum Name/Location	ID
Ocean	71.57	R. F. Kokaly et al. (2017)	Seawater_Open_Ocean SW2 lwch BECKa AREF	SW1
Aspen	0.89	R. F. Kokaly et al. (2017)	Aspen Aspen-1 green-top ASDFRa AREF	Aspen-1
Engelmann Magnolia Grandiflora	0.89	R. F. Kokaly et al. (2017)	Engelmann-Spruce ES-Needls-1 ASDFRa AREF	ES-Needls-1
Adenostoma Fasciculatum	2.67	S. K. Meerdink et al. (2019)	Magnolia grandiflora	JPL231
Reddish brown fine sandy loam	0.81	S. K. Meerdink et al. (2019)	Adenostoma fasciculatum 1	VH217
Acacia Visco	1.89	S. K. Meerdink et al. (2019)	Reddish brown fine sandy loam	87P1087
Rangeland	2.24	S. K. Meerdink et al. (2019)	Acacia visco	JPL159
Wetland	9.13	R. F. Kokaly et al. (2017)	Rangeland L02-069 S00% G99% ASDFRa AREF	L02-069
Wheat Residue	0.3	R. F. Kokaly et al. (2017)	Wetland YNP-WT-1 AVIRISb RTGC	YNP-WT-1
Asphalt	2.59	J. S. Jennewein et al. (2024)	Wheat, Field Scale Cut Green	33
Antarctic	0.17	S. K. Meerdink et al. (2019)	Construction Asphalt	0674UUUASP
Sand	2.87	T. C. Grenfell et al. (1994)	Table. 6	—
	3.99	R. F. Kokaly et al. (2017)	Quartz GDS74 Sand Ottawa BECKc AREF	GDS74 Sand

Clouds play an important role in Earth’s energy balance (D. L. Hartmann et al. 1992; L. Kaltenegger 2017; E. F. Harrison et al. 1990; V. Ramanathan et al. 1989; B. A. Wielicki et al. 1995) and can significantly influence the observed spectra of a planet by obscuring surface features and reducing the path length of reflected light (G. Tinetti et al. 2006; L. Kaltenegger et al. 2007; L. Kaltenegger 2017; J. T. O’Malley-James & L. Kaltenegger 2018b; F. Wang et al. 2022; J. Gomez Barrientos et al. 2023; S. R. Borges et al. 2024). We model the clouds as a slab of uniformly mixed H₂O particles that cover a fraction f_{cloud} of our atmosphere. The cloud structure in our simulations is defined by a top-of-cloud pressure $\log_{10} P_{\text{top}}$, cloud thickness $\Delta \log_{10} P$, mixing ratio $\log_{10}^{\text{aero}} \text{H}_2\text{O}$, and aerosol mean particle radius r_m . The optical properties of the clouds are precomputed in POSEIDON using Mie theory (G. Mie 1908) with precomputed aerosol properties from *mipython* (W. J. Wiscombe 1979; S. Prahl 2024). We adopt Mie-scattering properties for liquid H₂O clouds using refractive indices (G. M. Hale & M. R. Querry 1973) provided in the aerosol database (H. R. Wakeford & D. K. Sing 2015; E. Mullens et al. 2024) native in POSEIDON ($\geq v1.2$). A full description of POSEIDON’s cloud treatment can be found

in E. Mullens et al. (2024); E. Mullens & N. K. Lewis (2025).

In our forward-modeled reflection spectra, we assume the cloud slab has a mixing ratio of $\log_{10}^{\text{aero}} \text{H}_2\text{O} = -3$ and that the particles have a mean radius of $r_m = 1 \mu\text{m}$. The top of the cloud slab rests at a pressure of $P_{\text{top}} = 0.5$ bar and extends down to 0.6 bar for a thickness of 0.1 bar, such that $\Delta \log_{10} P = \log_{10}(0.6/0.5)$ bar. We generate spectra for three f_{cloud} scenarios: 0%, 50%, and 100%. POSEIDON computes fractional cloud coverage for reflected-light models by computing two spectra, one clear and one cloudy, and then taking the average of the two. Thus, the 50% cloud-coverage spectrum is obtained by equally weighting the 0% and 100% spectra. We note that given a planet in the habitable zone of its host star with a significant liquid-water ocean and secondary atmosphere, it is unlikely for the atmosphere and observed planet surface to be completely cloud-free, and 0% cloud-coverage case is included exclusively for modeling purposes.

2.2. MODIS Surface

We compute the surface albedo for a modern Earth using MODIS aboard NASA’s *Terra* and *Aqua* satel-

Table 3. Earth fractional coverage using IGBP classification scheme and the spectra used to represent each component. Spectra were primarily sourced from USGS (R. F. Kokaly et al. 2017) and ECOSTRESS (S. K. Meerdink et al. 2019), with the exception of snow (T. C. Grenfell et al. 1994) and cropland (J. S. Jennewein et al. 2024). Multiple spectra types under the “Spectral Representation” column indicate an equal weighting of the spectra.

IGBP Classification	(%)	Spectral Representation	Spectra Reference
Water	71.57	Ocean	R. F. Kokaly et al. (2017)
Evergreen Needleleaf Forest	0.49	Engelmann	R. F. Kokaly et al. (2017)
Evergreen Broadleaf Forest	2.36	Magnolia Grandiflora	S. K. Meerdink et al. (2019)
Deciduous Needleleaf Forest	0.09	Engelmann	R. F. Kokaly et al. (2017)
Deciduous Broadleaf Forest	0.58	Aspen	R. F. Kokaly et al. (2017)
Mixed Forest	0.93	Engelmann, Aspen, Magnolia Grandiflora	R. F. Kokaly et al. (2017); S. K. Meerdink et al. (2019)
Closed Shrubland	0.12	Adenostoma fasciculatum, Reddish brown fine sandy loam	S. K. Meerdink et al. (2019)
Open Shrubland	2.57	Adenostoma fasciculatum, Reddish brown fine sandy loam	S. K. Meerdink et al. (2019)
Woody Savanna	2.24	Acacia Visco	S. K. Meerdink et al. (2019)
Savanna	3.14	Rangeland	R. F. Kokaly et al. (2017)
Grassland	5.99	Rangeland	R. F. Kokaly et al. (2017)
Permanent Wetland	0.30	Wetland	R. F. Kokaly et al. (2017)
Cropland	2.31	Fresh Cut Wheat Residue	J. S. Jennewein et al. (2024)
Urban and Built-Up	0.17	Asphaltic Concrete	S. K. Meerdink et al. (2019)
Cropland/Natural Vegetation Mosaic	0.28	Fresh Cut Wheat Residue	J. S. Jennewein et al. (2024)
Snow and Ice	2.87	Antarctic	T. C. Grenfell et al. (1994)
Barren or Sparsely Vegetated	3.99	Quartz Ottawa Sand	R. F. Kokaly et al. (2017)

lites. We use land-cover maps based on the International Geosphere-Biosphere Programme (IGBP) classification scheme from the MODIS Land Cover Climate Modeling Grid Product (v6.1; MCD12C1) (M. Friedl & D. Sulla-Menashe 2022). The MCD12C1 science product provides annual global land-cover classifications at a 0.5-degree spatial resolution for 2001-2023. Due to potential issues with the MCD12Q1 land product data after 2021², from which MCD12C1 is derived, we aggregate annual data from 2010 through the end of 2020. We compute a latitudinally cosine-weighted average of surface coverage fraction across the 11 years of data.

Table 3 shows the IGPS classification scheme and surface coverage from the MODIS observations. We assign one or more reflection spectra to represent each classification category. The spectra we acquired are shown in Table 2 along with their fractional contribution to

the surface reflectance spectra, shown in black in the top panel of Fig. 1 (B). The total contribution to the surface spectra of components that have chlorophyll-induced features (Aspen, Engelmann, Magnolia Grandiflora, Adenostoma Fasciculatum, Acacia Visco, Rangeland, Wetland, and Wheat Residue) is 19.52%, or $f_{\text{forest}} \approx 0.20$. Sand and Reddish brown fine sandy loam, which share a similar spectral structure, have a combined coverage of 6.05%, or $f_{\text{sand}} \approx 0.06$. Both of these rougher classifications are used solely to analyze the MODIS-based model’s retrieval results. Following the classification scheme in B. Hapke (2012), the lab-derived spectra used to compute the disc-integrated reflection of exoplanets should be in the form of r_{dh} . However, commonly used databases, such as USGS (R. F. Kokaly et al. 2017) and ECOSTRESS (S. K. Meerdink et al. 2019), are constrained by laboratory data-collection methods designed for Earth and planetary science applications. While the difference is often small, it can lead to under-

² NASA LDOPE Case Name: [HC_MCD_24254](#)

or overestimation of the total reflectance (see Appendix A of E. Mullens et al. (2026, Submitted)).

The atmosphere model we used was generated using the well-tested and validated coupled 1D photochemistry and radiative transfer code `EXO-Prime` (L. Kaltenegger et al. 2007; S. Rugheimer et al. 2013, 2015; L. Kaltenegger et al. 2020a; J. Madden & L. Kaltenegger 2020a,b; L. Kaltenegger et al. 2020b). We adapt the P-T and chemical mixing profile from L. Kaltenegger et al. (2020a) for an Earth twin orbiting a Sun-like star, shown in panel (A) of Fig. 1. While the original chemical profile contained significantly more molecules, we included only molecules for which opacity data are available in `POSEIDON` and are spectrally prevalent between 0.4 and 1.8 μm . We include O_2 , H_2O , CH_4 , CO , and N_2O opacities from `HITRAN` (I. E. Gordon et al. 2017; I. E. Gordon et al. 2022) and O_3 from A. Serdyuchenko et al. (2014), in addition to $\text{N}_2\text{-N}_2$, $\text{N}_2\text{-H}_2\text{O}$, $\text{O}_2\text{-O}_2$, and $\text{O}_2\text{-N}_2$ CIAs (T. Karman et al. 2019), using `POSEIDON`'s temperate opacity database (Z. Lin et al. 2021). For consistency, the clouds are modeled identically to the `POSEIDON` consistent case in Sec. 2.1 with $f_{\text{cloud}} = 0.5$.

2.3. MYSTIC Model

The final spectrum in our modeling set was computed by G. Roccetti et al. (2025) using a complex, three-dimensional Earth model. The surface prescription of this Earth model was computed using the Hyperspectral Albedo Maps dataset with high Spatial and TEmporal Resolution (`HAMSTER`) (G. Roccetti et al. 2024). Clouds are modeled using a 3D Cloud Generator algorithm based on liquid and ice water content data from the European Centre for Medium-Range Weather Forecast's ERA5 reanalysis product (H. Hersbach et al. 2020). The spectrum was computed using the 3D Monte Carlo radiative transfer code `MYSTIC`. For more details on the creation of these spectral products, see G. Roccetti et al. (2025).

While G. Roccetti et al. (2025) provides spectra at various orbital configurations, we specifically requested a spectrum at full orbital phase ($\alpha = 0^\circ$) and with $\sim 50\%$ cloud coverage to remain consistent with the rest of our analysis. For this spectrum, the 3D model's viewing geometry yielded a surface composition of 43.9% land and 56.1% ocean. The land fraction is roughly 32.9% forest, 10.1% desert, and 0.4% ice. Ice and water clouds cover 41.4% and 47.5% of the visible planet's surface, respectively, and collectively cover 52.9% of the visible planet. The vertical molecular mixing ratio and P-T profile of these atmosphere models are based on the US standard atmosphere (G. P. Anderson et al. 1986).

2.4. Simulating HWO Observations

The EAC 5 design features 37 hexagonal segments with a circumscribed diameter of $D_{\text{circ}} = 10$ m and an inscribed diameter of $D_{\text{in}} = 8.3$ m. Each hexagonal segment is 1.65 m from point to point, arranged in three rings of mirrors surrounding the central segment, with a physical gap of 4 mm between adjacent segments. We model the EAC 5 aperture with `HCIPy` (E. H. Por et al. 2018), as shown in the inset of panel (A) of Fig. 2. Table 4 lists all observatory parameters used to model the EAC 5. The collecting area of the 37 hexagonal segments is $A = 65.4$ m², equivalent to an unobstructed circular pupil of diameter 9.12 m. To account for reflectivities in the mirrors, we assume the EAC 5 optical path is identical to the design published in the GOMAP Science-Engineering Interface repository³. We multiply the transmission and reflectivity of each optical element to acquire the total optical throughput $\mathcal{T}(\lambda)$, shown in panel (B) of Fig. 2.

2.4.1. Coronagraph Instrument

One of the key design choices shaping the science yield of HWO will be the CI. Here we model the HWO coronagraph as a Charge-6 Vector Vortex Coronagraph (`VVC-6`), which was considered for the `LUVOIR` (The `LUVOIR Team` 2019) and `HabEx` (B. S. Gaudi et al. 2020) mission designs. We use the `HCIPy` (E. H. Por et al. 2018) implementation of the `VVC-6` and a Lyot stop that is 85% of D_{circ} to model the point spread function (PSF). Note that we do not include a custom apodizing mask or any speckle reduction from the deformable mirrors, which would reduce contrast to the 10^{-10} level required to image an Earth twin. Thus, in our analysis, we set the core contrast to $C = 10^{-10}$, independent of the source's angular separation.

To compute the core throughput τ_{core} , we propagate the PSF of the source on- and off-axis. We compute the broadband PSF by sampling 11 wavelengths from a box bandpass centered at 0.5 μm with a 10% bandwidth. We adopt the same focal ratio as the EAC 1 design, $F/\# = 20$, defined as the ratio of the focal length to diameter. We assume the focal plane is Nyquist sampled, with a maximum separation of $32 \lambda/D$. An example of the on-axis PSF response of our modeled EAC 5 CI is shown in panel (C) of Fig. 2, with an off-axis source at $16 \lambda/D$ shown in panel (D).

We compute τ_{core} by performing aperture photometry using a circular aperture with radius $\sqrt{2}/2 \lambda/D$. We utilize the exoplanet mission simulation package

³ <https://github.com/HWO-GOMAP-Working-Groups/Sci-Eng-Interface>

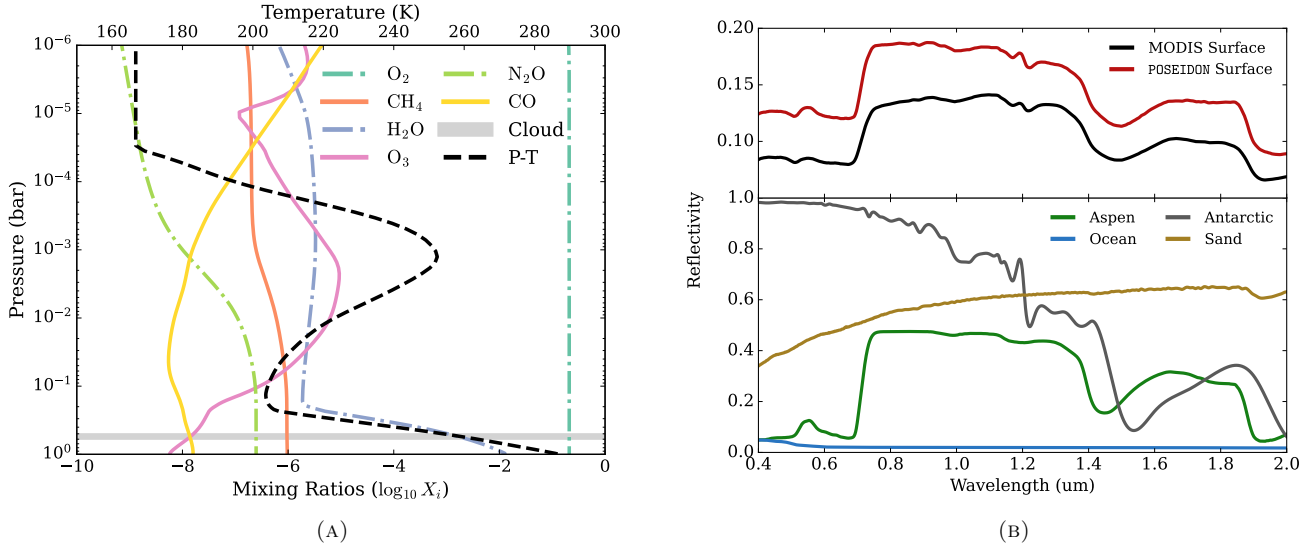


Figure 1. (A) P-T and chemical mixing ratio profile from [L. Kaltenecker et al. \(2020a\)](#) used in the MODIS-derived surface coverage model. Solid and dashed-dotted curves show the vertical mixing ratios of the molecular species contributing to the spectra. The dashed black line represents the P-T profile, and the gray horizontal bar indicates the water cloud height and thickness. (B) The top panel shows the surface spectra derived from MODIS observations, as outlined in [Sec.2.2](#), as well as the simpler four-component surface model for the three self-consistent **POSEIDON** spectra. The bottom panel shows the four spectra used in the three self-consistent forward models and in all retrievals.

Table 4. Parameters assumed for modeling the HWO EAC 5 design. Values are adopted from the GOMAP Science-Engineering Interface repository if available and filled with values from the LUVOIR report ([The LUVOIR Team 2019](#)).

Parameter	Description	Unit	VIS	NIR
D_{circ}	Circumscribed diameter	m		10
D_{in}	Inscribed diameter	m		8.3
A	Collecting area	m^2		65.4
C	Coronagraph design contrast	—		10^{-10}
\mathcal{R}	Spectral resolution	—	140	70
$[\lambda_{\text{min}}, \lambda_{\text{max}}]$	Wavelength range	μm	[0.4,1.0]	[1.0,1.8]
θ_{OWA}	Outer working angle	λ/D		32
θ_{IWA}	Inner working angle	λ/D		2.5
f_{PP}	Post-processing factor	—		0.1
T_{sys}	Telescope temperature	K		270
t_{exp}	Exposure time	hr		100
t_{read}	Read time	s		1000
R_{e^-}	Read noise	e^-/pixel	0	0.4
D_{e^-}	Dark current	$e^-/\text{pixel}/\text{s}$	3×10^{-5}	1×10^{-4}
R_C	Clock induced charge	e^-/pixel		1.3×10^{-3}

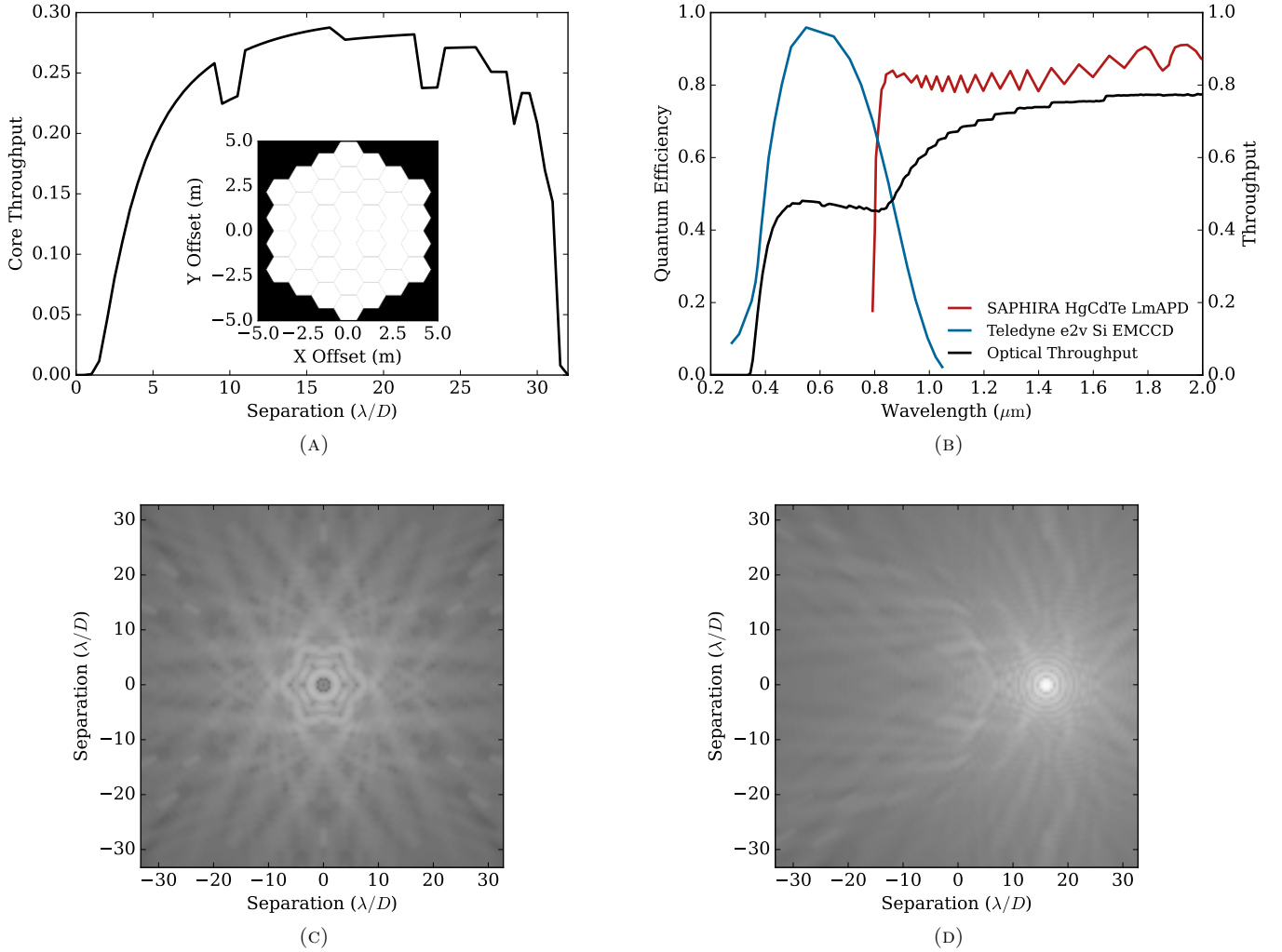


Figure 2. (A) Coronagraph core throughput τ_{core} and aperture of the EAC 5 design. (B) Optical throughput \mathcal{T} and quantum efficiency q used to model the HWO EAC 5. \mathcal{T} was computed using the full EAC 1 optical path, as specified by the HWO GOMAP Science-Engineering Interface. We acquired the QE values for Teledyne e2v EMCCD (VIS) and the SAPHIRA HgCdTe LmAPD (NIR) from the GOMAP Science-Engineering Interface repository. (C) On-axis PSF of the EAC 5 aperture shown in (A). (D) Off-axis PSF of the EAC 5 aperture shown in (A) at a separation of $\lambda/D = 16$.

EXOSIMS (D. Savransky & D. Garrett 2016; C. Delacroix et al. 2016) to process the off-axis PSF cube into the coronagraphic throughput shown in panel (A) of Fig. 2. We also assume quantum efficiencies $q(\lambda)$ of the VIS and NIR IFS. Panel (B) in Fig. 2 shows the assumed $q(\lambda)$ for the Teledyne e2v EMCCD (VIS) and the SAPHIRA HgCdTe LmAPD (NIR), acquired from the GOMAP Science-Engineering Interface repository.

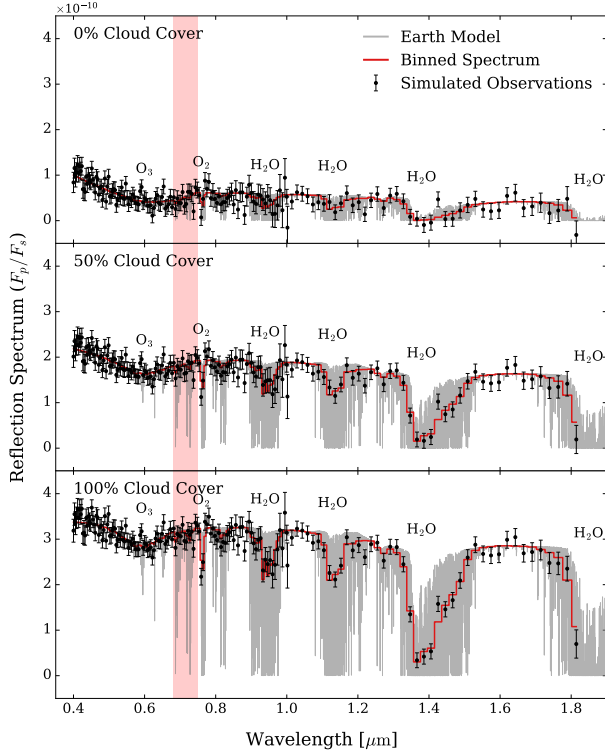


Figure 3. Simulated $t_{\text{exp}} = 100$ hr. observation at $\alpha = 90^\circ$ of the self-consistent POSEIDON spectra where the light gray curve denotes the high resolution ($\mathcal{R} = 10^4$) forward model, the black points denote the data from the simulated HWO EAC 5 observations, and the red step curve shows the high-resolution model binned down to the simulated observation wavelength bins. Gas-phase atmospheric absorption features for H_2O , O_2 , and O_3 are labeled along with the location of the red edge (red bar). The top, middle, and bottom panels are for the $f_{\text{cloud}} = 0, 0.5, \text{ and } 1.0$ cases, respectively.

2.4.2. Photon Counting

We estimate photon-counting errors in our simulated spectra using a modification of the noise routines included in the `coronagraph` package (J. Lustig-Yaeger et al. 2019), which are based upon the implementations of R. A. Brown (2005); C. C. Stark et al. (2014); T. D. Robinson et al. (2016). For a given exposure time t_{exp} , we compute the signal-to-noise ratio (SNR) (D. Garrett

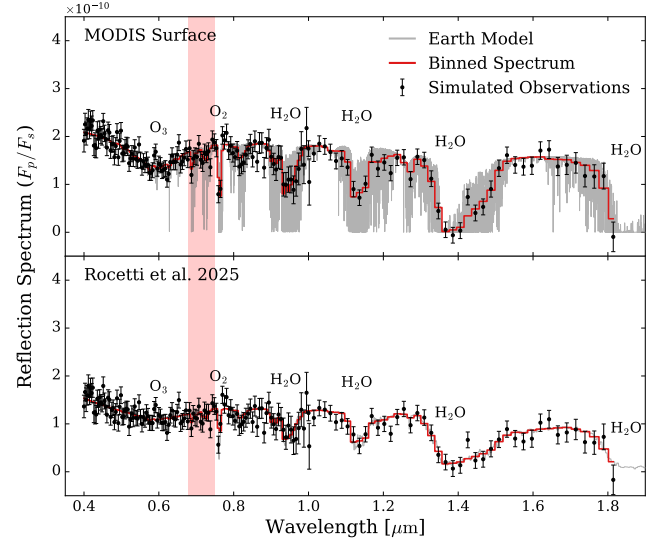


Figure 4. Simulated $t_{\text{exp}} = 100$ hr. observation at $\alpha = 90^\circ$ of the two complex spectral models. The light gray curve shows the high resolution ($\mathcal{R} = 10^4$) MODIS-derived forward-modeled spectra and the spectra from G. Rocetti et al. (2025) in the top and bottom panels, respectively. The black points denote the data from the simulated HWO EAC 5 observations and the red step curve shows the model spectrum binned down to the simulated observation wavelength bins. Gas-phase atmospheric absorption features for H_2O , O_2 , and O_3 are labeled along with the location of the red edge (red bar).

et al. 2017) of the observation as

$$\text{SNR}(t_{\text{exp}}) = \frac{c_p}{\sqrt{(c_p + c_b)/t_{\text{exp}} + c_{sp}^2}}, \quad (5)$$

where noise in the photon count rate from the planet c_p , all background sources c_b , and variance in the speckle residual c_{sp} are considered. The background count rate is composed of

$$c_b = c_z + c_{ez} + c_{sr} + c_{DC} + c_{RN} + c_{CIC} + c_{th}, \quad (6)$$

where c_z and c_{ez} are count rates from zodiacal and exozodiacal dust, respectively. The residual starlight that doesn't get suppressed by the optical system is given by c_{sr} . Count rates from the telescope and detector are accounted for via dark current c_{DC} , read noise c_{RN} , clock-induced-charge c_{CIC} , and thermal contributions c_{th} . The specific forms we adopt for each count-rate term are outlined in Appendix A.

Single-draw Gaussian noise can be used to simulate the variation in an observation accurately. We randomly sample a Gaussian distribution $\mathcal{N}(\mu, \sigma^2)$ to simulate a single-visit HWO observation, where the mean

$\mu = (F_{p,\lambda}/F_{s,\lambda})$ is the modeled spectra and the standard deviation $\sigma = (F_{p,\lambda}/F_{s,\lambda})/\text{SNR}(t_{\text{exp}})$ is computed from our noise model. For the HWO EAC 5 scenario we model, we assume an exposure time of $t_{\text{exp}} = 100$ hours. Previous work has noted the bias that single-draw Gaussian noise can introduce into retrievals with low spectral resolution (Y. K. Feng et al. 2018). A shift in a small cluster of data points, particularly near characteristic absorption or reflection bands, can significantly affect retrieval results. To investigate the effects of the single-draw Gaussian noise on our retrieval algorithm, we performed an additional retrieval with the $f_{\text{cloud}} = 0.5$ model, fixing the noise onto the true flux values with errors set by the SNR. We outline the results of this retrieval in Appendix B and note that it ultimately did not affect the results of the retrieval. Thus, to simulate a single observation using HWO, we proceed with the Gaussian noise draw.

Figs. 3 and 4 present our simulated 100-hour observations for the HWO EAC 5 design outlined above, for each spectral model. The gray curves in Fig. 3 and the top panel of Fig. 4 denote the high-resolution ($\mathcal{R} = 10^4$) spectra we created using the Earth models outlined in Secs. 2.1 and 2.2. The gray curve in the bottom panel of Fig. 4 shows the model from G. Rocchetti et al. (2025) with a constant wavelength bin width of $\Delta\lambda = 1$ nm. The red step curves show the spectra binned down to $\mathcal{R} = 140$ and $\mathcal{R} = 70$ in the VIS (0.4-1.0 μm) and NIR (1.0-1.8 μm), respectively, with the simulated observations in black points with symmetric errors given by $\sigma_\lambda(t_{\text{exp}})$.

The individual noise terms used to compute the SNR, as outlined in Appendix A, are shown in Fig. 5 for the MODIS-derived spectra. Individually, photons from the stellar residual c_{sr} and exozodiacal dust c_{ez} contribute significant portions of the background c_{b} . Due to the choice of detector technologies, read noise is absent in the VIS but contributes significantly in the NIR. Thermal effects from the observatory are only noticeable at the reddest wavelengths, resulting in an increase in c_{b} . Photons from the planet, shown by the solid black curve in Fig. 5, also consistently remain within an order of magnitude of c_{b} .

Variations in the stellar residual c_{sr} dominate the noise in the observed spectra when the exposure time increases significantly, as shown in Eqn. A10. When contributions from speckle residual variations dominate the observation noise, any increase in t_{exp} will not improve the SNR. We denote this turnover as the saturation time t_{sat} . The saturation time is set by finding the

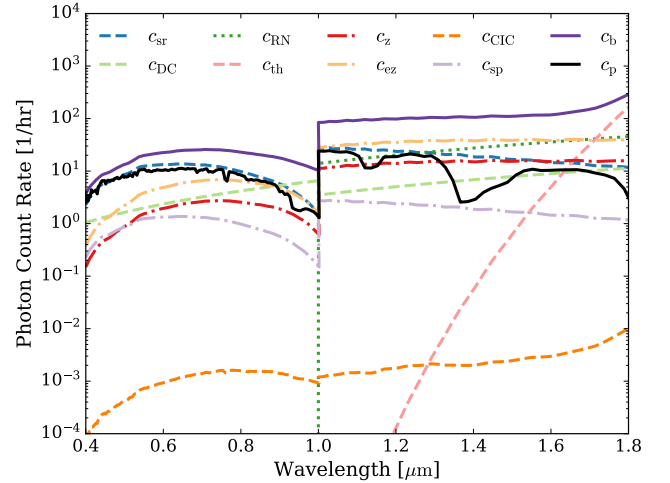


Figure 5. Individual photon count rates for the MODIS-derived spectra. The forms of the count rates are outlined in App. A. The planet count rate is consistently within an order of magnitude of the total background except at the reddest wavelengths.

t_{exp} that satisfies

$$(c_{\text{p}} + c_{\text{b}})/t_{\text{exp}} = c_{\text{sp}}^2. \quad (7)$$

For our observatory model, target system, and expected post-processing ability, we find a median saturation time of $\tilde{t}_{\text{sat}} = 32$ hrs for the MODIS-derived spectra. For the observing scenario considered in our work, a 100-hr exposure time greatly reduces the noise in c_{p} and c_{b} , ensuring that we are near the noise floor for most of the spectral coverage. Fig. 6 shows contributions to the SNR from c_{p} and c_{b} scaled by t_{exp} and the noise floor c_{sp}^2 for the MODIS-derived spectra. Dashed and dotted curves show the 100 hr exposure time used to simulate observations in our work and the median saturation time of 32 hrs, respectively. Except near 1 μm in the VIS, where the QE of the Teledyne e2v EMCCD degrades, and toward 1.8 μm , where thermal effects become significant, c_{sp} dominates noise in the observed spectrum. At the median saturation time, we find that c_{sp} dominates the spectra except where the QE of the EMCCD, shown in panel (B) of Fig. 2, drops significantly in the VIS. In the NIR, the combination of thermal effects towards 1.8 μm and the decrease in photon counts from the stellar residual c_{sr} relative to the other photon sources results in the turnover at 1.4 μm .

2.5. Retrieval

We use the same retrieval setup for each simulated observation. We assume uniform mixing ratios of H_2O , O_3 , and O_2 and an isothermal atmosphere. In the initial

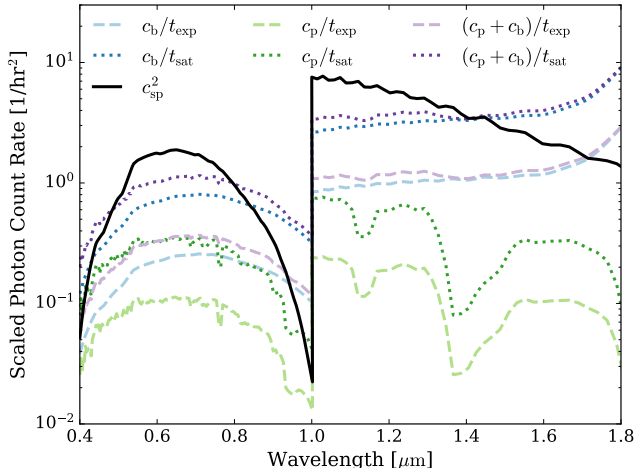


Figure 6. Photon noise contributions to the simulated observations from the planet and all background sources scaled by the t_{exp} . The solid black curve shows the square of photon counts from variations in the speckle residual, c_{sp} , which serves as the observational noise floor. Dashed curves show the scaled count rates from the nominal exposure time of $t_{\text{exp}} = 100$ hr. The dotted curves show where t_{exp} sets the median of c_{sp}^2 equal to the median of $(c_b + c_p)/t_{\text{exp}}$, denoted as the saturation time t_{sat} . For our observatory configuration and $f_{\text{pp}} = 0.1$, the median saturation time is $t_{\text{sat}} = 32$ hrs.

stages of this study, we utilized a more complex, two-gradient P-T profile (R. J. MacDonald & N. K. Lewis 2022) to retrieve atmospheric structure. We found that the two-gradient P-T profile produced an isothermal atmosphere regardless of the spectral model, motivating our decision to use an isothermal atmosphere to reduce the retrieval dimensionality. Clouds are defined by a uniformly mixed slab of Mie-scattering H_2O molecules in our simulations. We set the fractional coverage for the four surface spectra shown in panel (B) of Fig. 1 as free parameters in the retrieval. We sample the atmosphere using the same custom 200-layer pressure grid as in the forward models. This parameterization is identical to the three forward-modeled spectra we computed solely within POSEIDON, as outlined in Sec. 2.1. During the retrieval process, we compute spectra at high spectral resolution ($\mathcal{R} = 10^4$) and down-sample them to the simulated observing wavelengths.

We assume semi-informed priors for R_p and $\log_{10} P_{\text{surf}}$. The $\mathcal{U}(-3, 2)$ prior on $\log_{10} P_{\text{surf}}$ is informed by the ~ 1 mbar Martian and ~ 100 bar Venusian surfaces. The determination of R_p is unfeasible for photometric observations alone. Given multiple epochs of photometric observations at different orbital phases and assuming the orbital parameters of the planet are well constrained, R_p may be constrained to within a factor

of 2 of its actual value (B. S. Gaudi et al. 2020). This would enable tighter prior bounds on R_p , but ultimately rely on the determination of $\Phi(\alpha)$ and r_p . Thus, we are unable to place tight priors on R_p , and assume a conservative, broad $\mathcal{U}(0.1, 10)$ prior on R_p roughly informed by exoplanet radius distributions (B. J. Fulton et al. 2017; R. K. Kopparapu et al. 2018; A. R. Neil & L. A. Rogers 2020). In Appendix C, we performed a retrieval using a tighter $\mathcal{U}(0.5, 2.0)$ prior on R_p for the $f_{\text{cloud}} = 0.5$ model and discussed it in the context of the $\mathcal{U}(0.1, 10)$ prior. The radius retrieved is the reference radius used to solve for hydrostatic equilibrium, which we set to the lower surface pressure prior limit of 1 mbar, and is not the radius at $\log_{10} P_{\text{surf}}$. To compute F_p/F_s , we set the radius of the reflecting surface as a wavelength-dependent photospheric radius, defined as the location where the optical depth reaches $\tau = 2/3$. Using the photospheric radius in emission spectrum retrievals has been shown to reduce biases in the location of the emitting surface (J. J. Fortney et al. 2019; J. Taylor 2022). The 13 other parameters are assigned uniform priors with limits that cover the space of likely parameter values, listed in Table 1, for a total of 15 free parameters in the retrieval.

POSEIDON performs Bayesian inference using the nested sampling algorithm PyMultiNest (J. Buchner et al. 2014; J. Buchner 2016), which is a Python wrapper of the widely used MultiNest (F. Feroz et al. 2009) software. We ran our retrievals using 2000 live points (N_{live}), which follows recommendations to utilize at least $N_{\text{live}} \geq 1000$ from the original MultiNest documentation (F. Feroz et al. 2009) and recent studies on the algorithm’s performance (A. Dittmann 2024). Each retrieval ran in parallel across 96 cores on Intel Xeon Platinum 8468H 64-bit processors. For a further description of the MultiNest setup used in this work, see R. J. MacDonald & N. Madhusudhan (2017).

3. RESULTS

We simulate the performance of HWO in identifying the surfaces and atmospheres of terrestrial exoplanets across models of increasing complexity using the open-source spectral-retrieval code POSEIDON. We begin with the three spectra parameterizations produced by POSEIDON’s forward model capabilities, which are identical to the retrieval parameterization. We then extend to two complex models that employ complex atmospheric and surface structures.

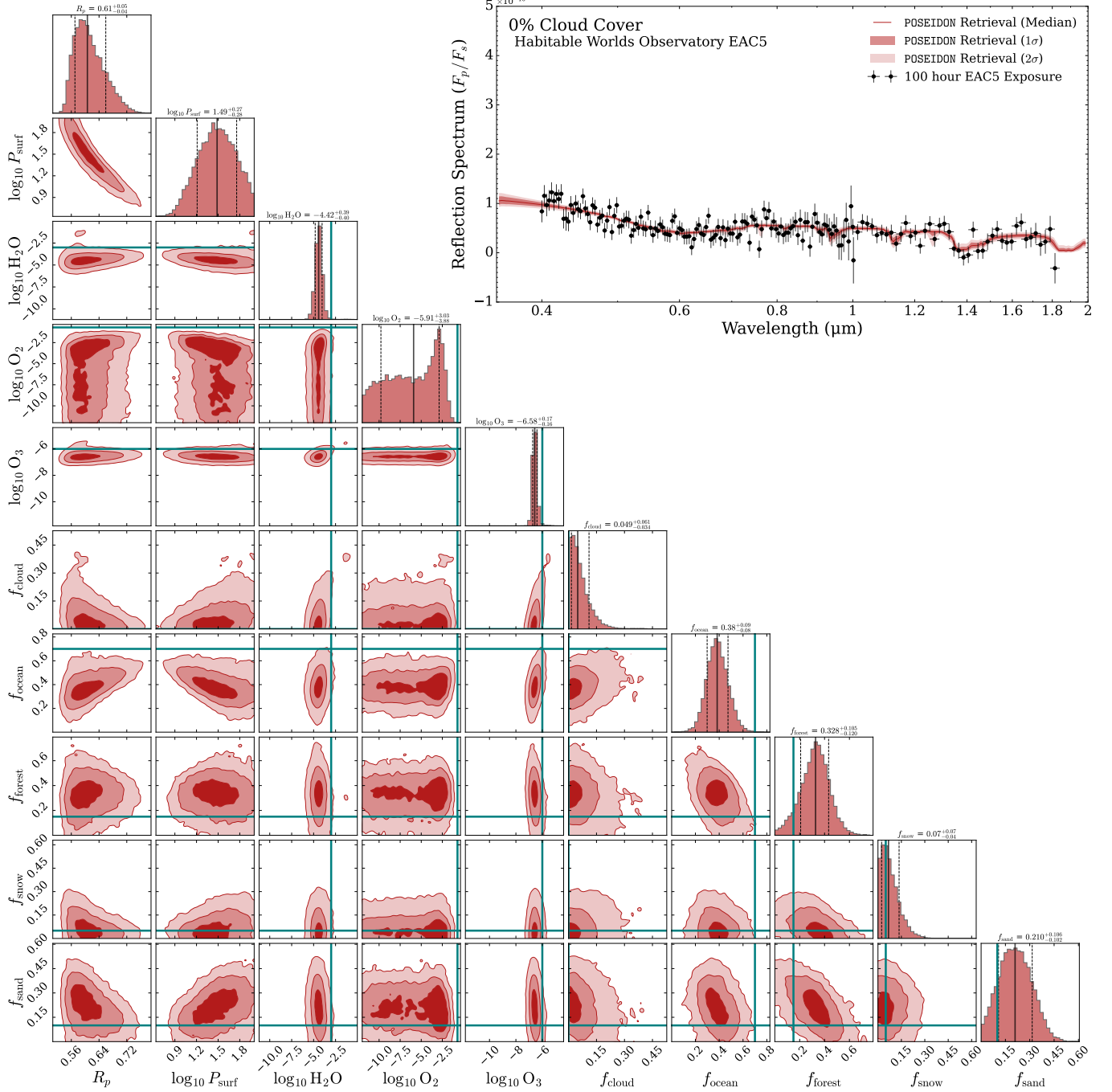


Figure 7. Retrieval results for the self-consistent POSEIDON spectra with 0% cloud coverage. The posterior distributions for selected parameters are shown on the left-hand side, along with the median-retrieved spectra and simulated data in the top-right panel. The marginalized median and 1- σ intervals for each parameter are labeled above the distributions and are shown in the black solid and dashed lines, respectively. The values used in the forward model, listed in Table 1, are shown by the solid teal line in the posteriors. The full posterior distribution is shown in Fig. 14.

3.1. POSEIDON *Consistent Spectra*

3.1.1. *Cloud-free*

Fig. 7 shows the observed and retrieved spectra for the 0% cloud coverage scenario. The retrieval confidently computes a cloud-free planet, with $f_{\text{cloud}} = 0.049^{+0.061}_{-0.034}$. In the absence of clouds, photons entering the atmosphere can reach the surface and be reflected back to the observer. The cloud-free case, although unlikely for an Earth-like planet in the HZ with a liquid-water ocean, provides complete spectral access to the surface. Classification of individual surface features, however, is dependent on proper constraints of R_p and $\log_{10} P_{\text{surf}}$. While the retrieval correctly identified a cloudless planet, a smaller rocky planet with $R_p = 0.63^{+0.05}_{-0.03}$ and a brighter surface was favored over a larger radius with a dimmer surface.

The degeneracies identified in the retrieval are evident in the posterior distributions of R_p shown in Fig. 7. As R_p decreases and dims the spectrum by reducing the reflecting surface area, a reduction in f_{ocean} and an increase in f_{sand} are necessary to normalize the spectrum to be equivalent to the data. The brighter surfaces were overestimated, with $f_{\text{forest}} = 0.328^{+0.105}_{-0.124}$ and $f_{\text{sand}} = 0.210^{+0.106}_{-0.102}$, while the ocean coverage of $f_{\text{ocean}} = 0.38^{+0.09}_{-0.08}$ was underestimated. The snow coverage was retrieved within $1\text{-}\sigma$ of its input value of 0.05, with $f_{\text{snow}} = 0.07^{+0.07}_{-0.04}$. The retrieval also preferred a larger surface pressure, with $\log_{10} P_{\text{surf}} = 1.54^{+0.22}_{-0.22}$. H_2O and O_3 were constrained with abundances of $\log_{10} \text{H}_2\text{O} = -4.42^{+0.29}_{-0.40}$ and $\log_{10} \text{O}_3 = -6.58^{+0.17}_{-0.16}$, lower than the forward model parametrization of -3 and -6, respectively. An upper limit on molecular O_2 was placed of $\log_{10} \text{O}_2 = -5.91^{+3.03}_{-3.88}$, which is significantly lower than the input abundance of -0.7. The inconsistency in O_2 is likely due to the random noise draw for the simulated observation, as one of the data points in the oxygen A band ($0.76 \mu\text{m}$) was shifted close to the continuum level. The planet's isothermal temperature was also significantly underestimated, and only a lower limit of $T = 213^{+105}_{-74}$ K could be established, as shown in the full corner plot in Fig. 14.

3.1.2. *Patchy Clouds*

Retrieval results of the 50% cloud coverage model are shown in Fig. 8. The retrieval model determined an upper limit of $f_{\text{cloud}} = 0.759^{+0.078}_{-0.167}$, indicating patchy cloud coverage. A lower limit on the planetary radius was placed with $R_p = 0.84^{+0.05}_{-0.02} R_{\oplus}$, larger than the radius found for the 0% cloud coverage model but still inconsistent with the $1 R_{\oplus}$ for Earth. The detection of clouds enabled the tighter constraints on R_p that are closer to $1 R_{\oplus}$, but a significant degeneracy be-

tween R_p and f_{cloud} is shown clearly in the posteriors in Fig. 8. The degeneracy between R_p and surface coverage was now accompanied by a degeneracy in cloud coverage; clouds attenuated the surface spectra and were used by the retrieval to brighten the spectra in place of R_p . This degeneracy with f_{cloud} is less pronounced than that associated with R_p , but it still affects the ability to constrain the surface accurately. All three land spectra were constrained consistently within their input values. We find that upper limits of $f_{\text{forest}} = 0.230^{+0.134}_{-0.138}$, $f_{\text{snow}} = 0.14^{+0.13}_{-0.09}$, and $f_{\text{sand}} = 0.241^{+0.134}_{-0.144}$ were placed in the retrieval, within $1\text{-}\sigma$ of their input values of 0.15, 0.06, and 0.10, respectively. However, the larger estimates of land fractions required a lower liquid-water ocean coverage, $f_{\text{ocean}} = 0.36^{+0.14}_{-0.13}$. We find that $\log_{10} \text{H}_2\text{O} = -3.16^{+0.42}_{-0.30}$, $\log_{10} \text{O}_2 = -1.14^{+0.42}_{-0.41}$, and $\log_{10} \text{O}_3 = -6.15^{+0.26}_{-0.23}$ were all consistent with the model inputs of -3, -0.7, and -6, respectively. The brighter continuum enhances the signal from molecular absorptions, enabling consistent constraints on gas-phase absorptions.

3.1.3. *Cloudy Day*

The retrieval results for the 100% cloud coverage model are shown in Fig. 9. We find significant cloud coverage in the simulated observation, with $f_{\text{cloud}} = 0.92^{+0.05}_{-0.20}$ of the atmosphere being covered. The increased continuum from the water clouds enabled $R_p = 1.03^{+0.01}_{-0.01}$ to also be constrained consistently with the $1 R_{\oplus}$ input. We find that the surface pressure is not as tightly constrained as R_p , with $\log_{10} P_{\text{surf}} = 1.13^{+0.53}_{-0.60}$. The significant cloud coverage prevents any photons from reaching the surface and reflecting to the observer. Thus, apparent constraints on the surface are not actually informed by the spectrum, and any apparent consistency with the inputs is coincidental. This can be seen clearly with $f_{\text{snow}} = 0.21^{+0.13}_{-0.13}$, which has very distinctive spectral features in the VIS and NIR, and was constrained correctly for both the 0% and 50% cloud coverage forward models. The gas-phase vertical mixing ratios $\log_{10} \text{H}_2\text{O} = -3.14^{+0.41}_{-0.31}$, $\log_{10} \text{O}_2 = -0.93^{+0.42}_{-0.37}$, and $\log_{10} \text{O}_3 = -6.21^{+0.26}_{-0.20}$ were all retrieved within $1\text{-}\sigma$ of the input values of -3, -0.7, and -6, respectively. Constant vertical mixing ratios across the entire pressure grid ensure that features stand out above the bright cloud deck, enabling strong detection.

3.2. *External Models*

Two retrievals were run on models in which the parameters used in the forward model do not perfectly match those in the retrieval. Thus, for the external models, we are looking to constrain specific patterns. For the atmosphere, we want to assess the detection

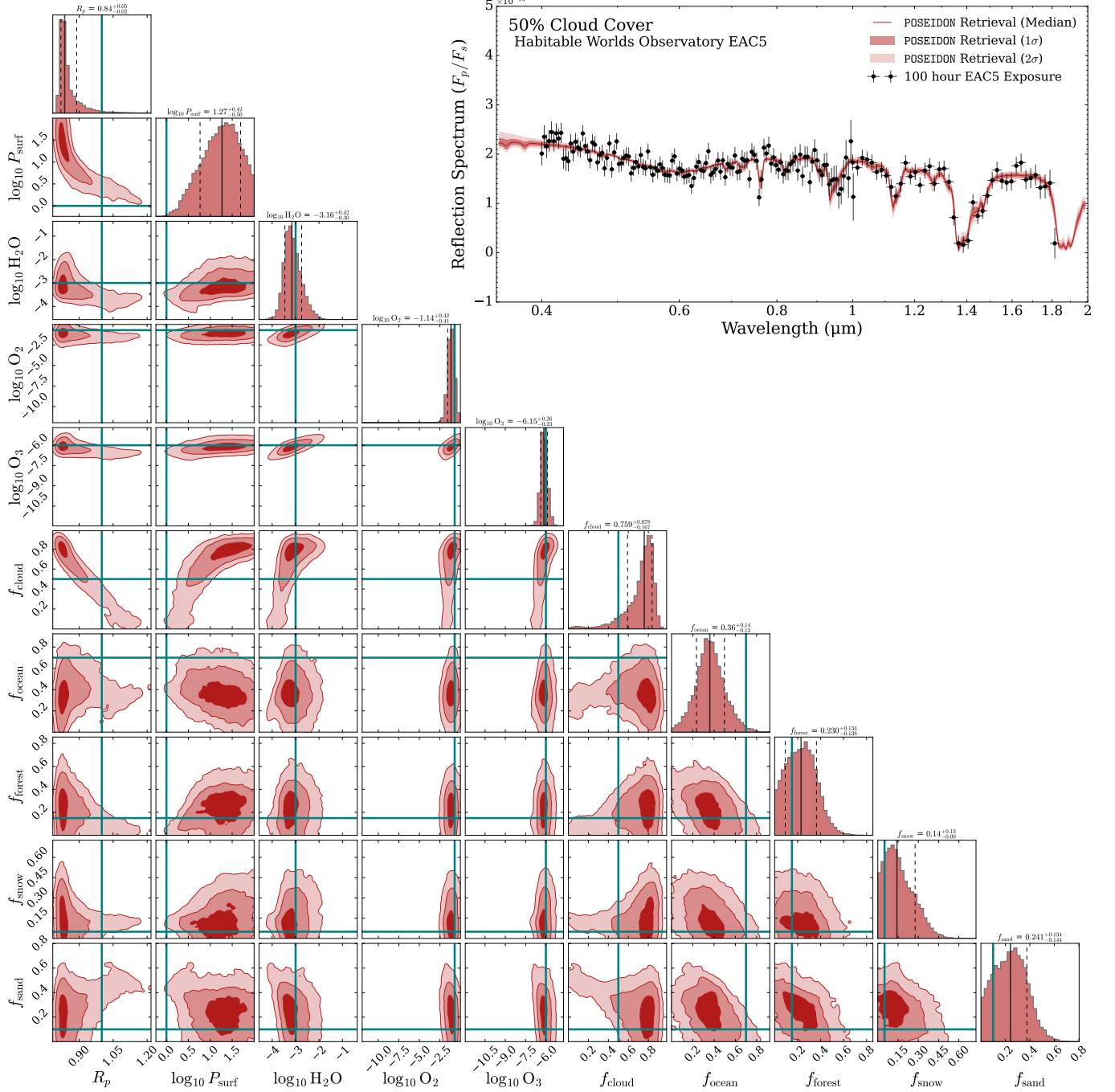


Figure 8. Retrieval results for the self-consistent POSEIDON spectra with 50% cloud coverage. The posterior distributions for selected parameters are shown on the left-hand side, along with the median-retrieved spectra and simulated data in the top-right panel. The marginalized median and 1- σ intervals for each parameter are labeled above the distributions and are shown in the black solid and dashed lines, respectively. The values used in the forward model, listed in Table 1, are shown by the solid teal line in the posteriors. The full posterior distribution is shown in Fig. 15.

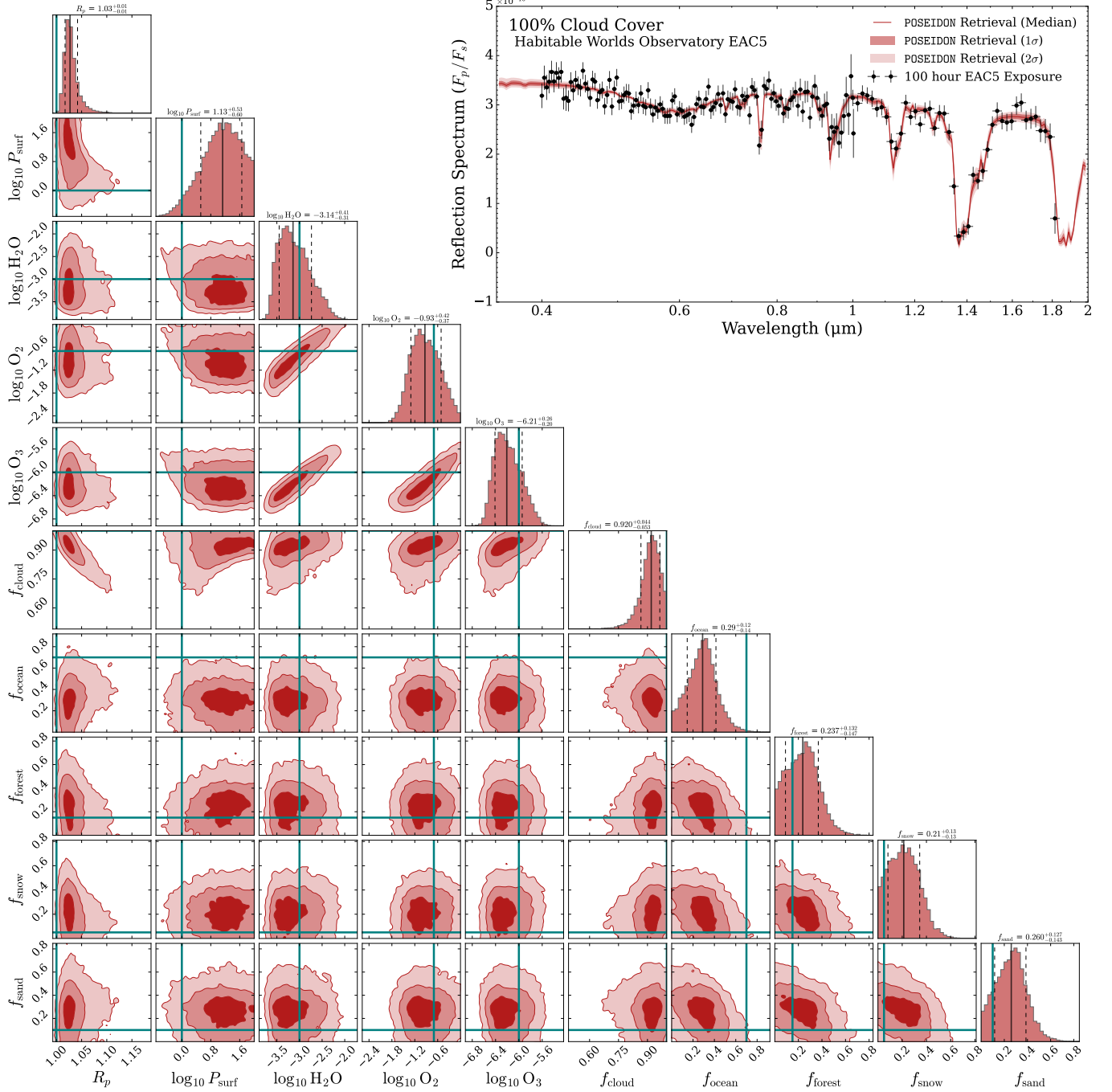


Figure 9. Retrieval results for the self-consistent POSEIDON spectra with 100% cloud coverage. The posterior distributions for selected parameters are shown on the left-hand side, along with the median-retrieved spectra and simulated data in the top-right panel. The marginalized median and 1- σ intervals for each parameter are labeled above the distributions and are shown in the black solid and dashed lines, respectively. The values used in the forward model, listed in Table 1, are shown by the solid teal line in the posteriors. The full posterior distribution is shown in Fig. 16.

of 50% cloud coverage in both models and atmospheric mixing ratios consistent with modern Earth conditions. For MODIS-derived spectra, and even more so for the MYSTIC spectra, we are not able to reproduce the input surface albedo perfectly. We aim to identify two characteristics: a significant liquid-water ocean and partial forest coverage. Constraining the planetary radius will also be necessary to place the cloud and surface properties in context.

3.2.1. MODIS Surface

The retrieval of simulated observations of the combined MODIS-derived surface spectra and L. Kaltenegger et al. (2020a) atmospheric profile Earth model is shown in Fig. 10. An upper limit on a patchy cloud slab was detected with a coverage of $f_{\text{cloud}} = 0.728_{-0.171}^{+0.086}$. We find a lower limit on the planetary radius of $R_p = 0.83_{-0.02}^{+0.06} R_{\oplus}$ and an overestimation of the surface pressure $\log_{10} P_{\text{surf}} = 1.16_{-0.46}^{+0.48}$ bar due to the increase in cloud coverage. Fig. 10 clearly shows the degeneracy between R_p , $\log_{10} P_{\text{surf}}$, and f_{cloud} ; if the cloud fraction were to have been at the 50% level consistent with the input model, the retrieval would've required a larger R_p and lower $\log_{10} P_{\text{surf}}$. We find that constant vertical mixing ratios used in the retrieval model accurately constrain the complex chemical mixing profile from L. Kaltenegger et al. (2020a), shown in Fig. 1. We detect $\log_{10} \text{H}_2\text{O} = -2.74_{-0.19}^{+0.23}$, consistent with the mixing ratio just above the cloud deck. Atmospheric mixing ratios for $\log_{10} \text{O}_2 = -0.63_{-0.22}^{+0.22}$ and $\log_{10} \text{O}_3 = -5.90_{-0.17}^{+0.15}$ were also consistent with the chemical profile used.

For this retrieval, ocean coverage was underestimated with $f_{\text{ocean}} = 0.37_{-0.13}^{+0.14}$ and sand surface coverage was overestimated with an upper limit of $f_{\text{sand}} = 0.231_{-0.141}^{+0.130}$ compared to their expected values of 0.716 and ~ 0.06 , respectively. As seen in Fig. 1, both the quartz sand and ocean spectra are relatively featureless between 0.4 and 1.8 μm . The increase in sand coverage and decrease in ocean coverage brightened the spectra, compensating for the smaller retrieved value of R_p . Chlorophyll features were accurately detected, with $f_{\text{forest}} = 0.225_{-0.137}^{+0.136}$ consistent with the expected coverage of ~ 0.20 . Snow coverage, while not consistent with the input value of 0.03, was disfavored by the retrieval and constrained to $f_{\text{snow}} = 0.14_{-0.09}^{+0.13}$.

3.2.2. MYSTIC Model

Results from the G. Rocchetti et al. (2025) spectral model retrieval are shown in Fig. 11. We find that the nested sampling required $f_{\text{cloud}} = 0.065_{-0.041}^{+0.059}$ to reproduce the flux of the planet, despite their ERA5-based clouds covering 52.9% of the model. In G. Rocchetti et al. (2025), the authors point out how zooming out

their 3D spectral grid to a single pixel (1D) spectra brightens their model. Thus, our 1D retrieval model may be systematically brighter than the 3D model used in G. Rocchetti et al. (2025), requiring lower cloud coverage to reproduce the flux. The marginalized median planetary radius of $R_p = 0.88_{-0.06}^{+0.06} R_{\oplus}$ from the retrieval is underestimated with respect to Earth. Atmospheric water vapor abundance was tightly constrained to $\log_{10} \text{H}_2\text{O} = -3.59_{-0.29}^{+0.29}$. O_2 was constrained to $\log_{10} \text{O}_2 = -2.08_{-0.75}^{+0.50}$ and an upper limit on O_3 was placed of $\log_{10} \text{O}_3 = -7.29_{-2.89}^{+0.63}$.

For the planetary surface, a liquid water ocean was detected at $f_{\text{ocean}} = 0.26_{-0.12}^{+0.08}$, inconsistent with the input surface ($f_{\text{ocean}} = 0.56$). Sand and snow coverage were significantly overestimated with $f_{\text{snow}} = 0.20_{-0.05}^{+0.05}$ and $f_{\text{sand}} = 0.313_{-0.061}^{+0.067}$ rather than the provided fractional coverages of 0.004 and 0.101, respectively. We underestimated the total forest cover, with the retrieved fraction of $f_{\text{forest}} = 0.234_{-0.088}^{+0.086}$ just short of 1- σ of the reference coverage of 0.329. The lower estimate of forest coverage is likely partly due to differences in our surface-spectral choices compared with those used by HAMSTER (G. Rocchetti et al. 2024). Laboratory and field measurements of individual materials are often conducted under ideal conditions, and do not capture the complex structure present in real observations of planets. G. Rocchetti et al. (2025) found that using biota spectra from USGS and ECOSTRESS spectra alone, which are common in Earth modeling and shown in Fig. 1, can overestimate the reflectance by up to a factor of ~ 2 in key bands compared to the more realistic HAMSTER models that account for this spatial complexity. Thus, our forest fraction likely needed to be lower to account for this difference.

4. DISCUSSION

We demonstrated that surface composition can be weakly constrained using atmospheric retrieval algorithms for single-visit VIS/NIR HWO EAC 5 spectroscopic observations. Previous analyses that retrieved wavelength-independent surface albedos consistently constrain surface pressure (Y. K. Feng et al. 2018; A. Salvador & T. D. Robinson 2025; E. Mullens et al. 2026, Submitted). Other research using agnostic or lab-based surface prescriptions has constrained surface pressure by employing broader spectral coverage in the UV and NIR (J. Gomez Barrientos et al. 2023; A. G. Ulses et al. 2025) and by using noise fixed to the true flux values (J. Gomez Barrientos et al. 2023; F. Wang et al. 2022; A. G. Ulses et al. 2025). For our VIS/NIR models (0.4-1.8 μm) with Gaussian scattered noise, we find that the surface pressure is overestimated across all observa-

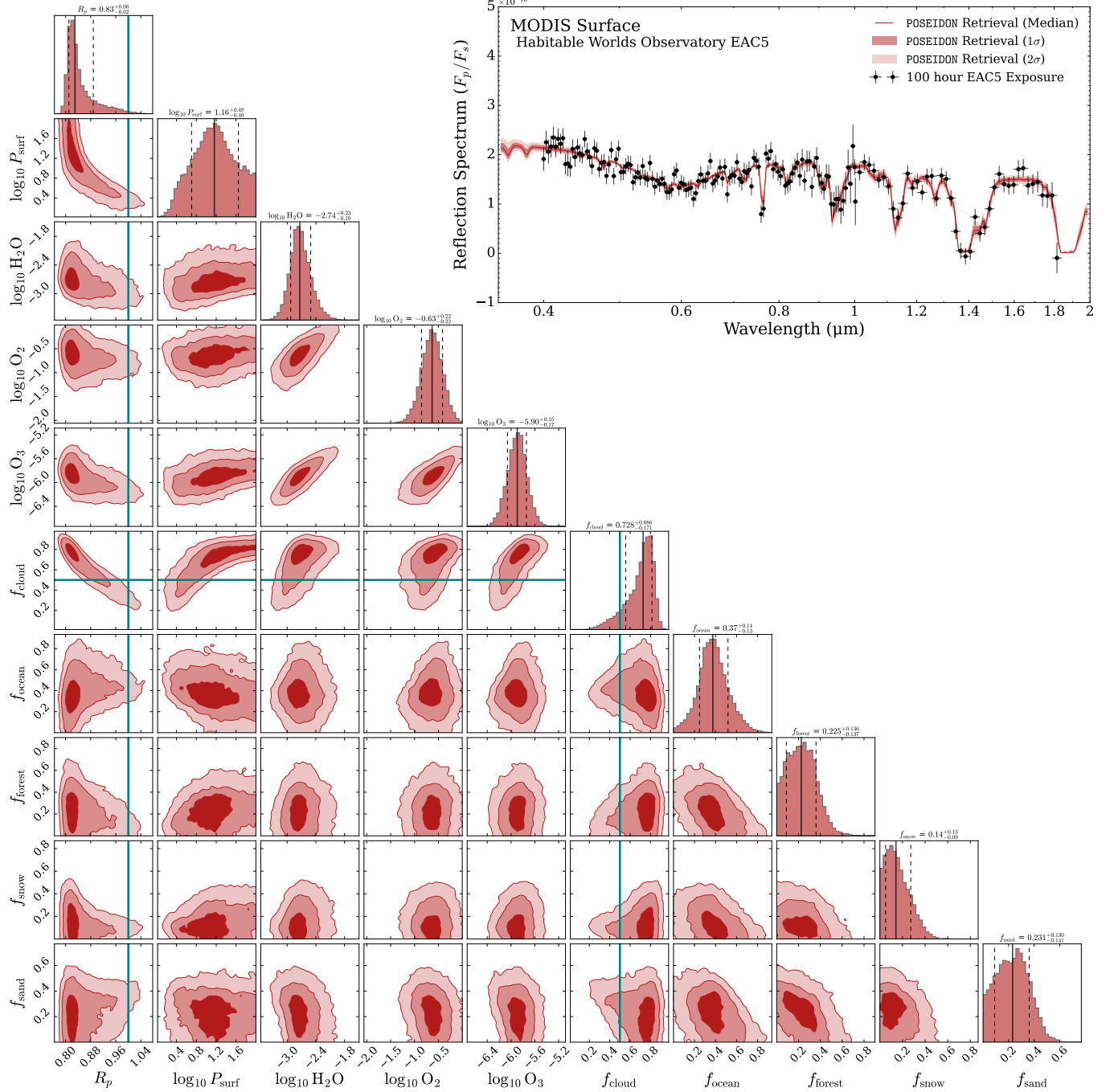


Figure 10. Retrieval results for the MODIS-derived spectral model. The posterior distributions for selected parameters are shown on the left-hand side, along with the median-retrieved spectra and simulated data in the top-right panel. The marginalized median and 1- σ intervals for each parameter are labeled above the distributions and are shown in the black solid and dashed lines, respectively. The values used in the forward model, where available, are shown by the solid teal line in the posteriors. The full posterior distribution is shown in Fig. 17.

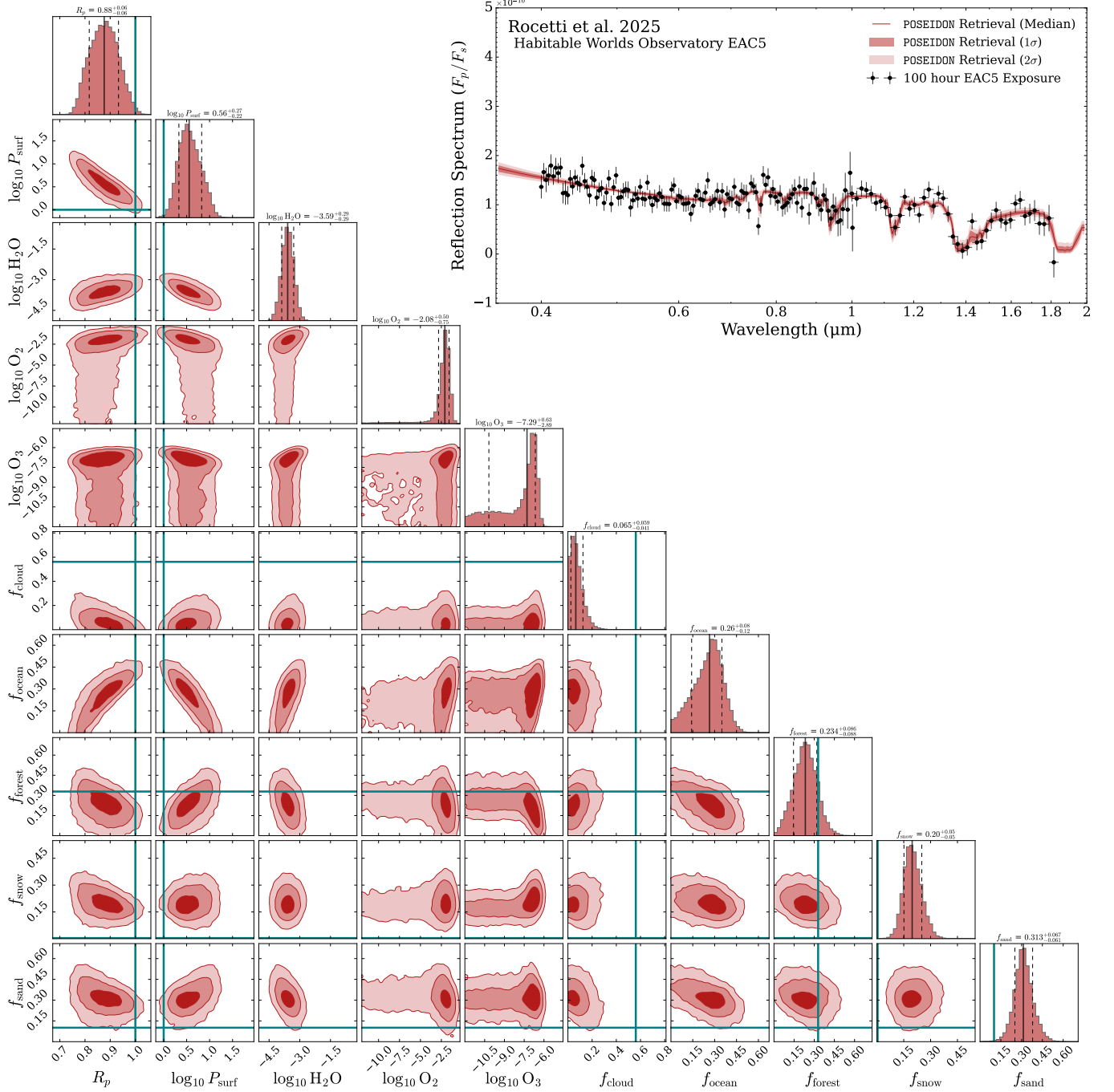


Figure 11. Retrieval results for the spectral model from G. Rocetti et al. (2025). The posterior distributions for selected parameters are shown on the left-hand side, along with the median-retrieved spectra and simulated data in the top-right panel. The marginalized median and 1- σ intervals for each parameter are labeled above the distributions and are shown in the black solid and dashed lines, respectively. The model parameterization provided by G. Rocetti et al. (2025) for specific variables, discussed in Sec. 2.3, is shown by the solid teal line in the posteriors. The full posterior distribution is shown in Fig. 18.

tion models and is degenerate with many free parameters in the retrieval, notably R_p and f_{cloud} .

Clouds play a unique role in both distinguishing and suppressing spectral signatures when modeling modern Earth’s atmosphere. While clouds significantly enhance the brightness of the planet, as can be clearly seen in Fig. 3, they mask surface features and can be degenerate with flatter surface spectra. Because clouds on Earth are near the surface in pressure space, they act as an opaque reflecting surface in the HWO wavelength range. They significantly complicate the classification of surface components on planets with moderate global cloud cover because they reflect photons that would otherwise interact with the planetary surface. Depending on cloud properties, such as height, thickness, aerosol abundance, and molecular size, any constraints on surface properties for a planet with significant cloud coverage may be unreliable. The planetary surfaces covered by optically thick H_2O clouds will not contribute to the observed spectra. On Earth, optically thick water clouds ($\tau_{\text{H}_2\text{O}} > 2$) cover a global average of $f_{\text{cloud}} = 0.56$ of the planet (C. J. Stubenrauch et al. 2013). Note that clouds cover the ocean around 10-15% more than land (C. J. Stubenrauch et al. 2013), potentially causing an overestimation in land coverage for patchy observations of Earth-like planets. However, we find the brighter continuum from thick, low-altitude clouds, which enabled tighter constraints on gas-phase absorption features above the cloud deck because gas-phase absorption generally imprints larger signals on highly reflective cloudy spectra than on cloudless ones.

The condensation of water vapor in Earth’s atmosphere plays an essential role in Earth’s energy balance and radiative forcing (D. L. Hartmann et al. 1992; L. Kaltenecker 2017; E. F. Harrison et al. 1990; V. Ramanathan et al. 1989; B. A. Wielicki et al. 1995). As shown in Fig. 1, gas-phase H_2O is removed from the atmosphere as it condenses into clouds. Previous work (M. Damiano & R. Hu 2022) attempted to account for this by introducing a condensation ratio, which reduces the volume mixing ratio of the gaseous species condensing into the atmosphere. Ref. M. Damiano & R. Hu (2022)’s study of terrestrial planets, however, found it difficult to constrain the H_2O condensation ratio. Further developing self-consistent techniques to integrate gas- and solid-phase abundances for future observations of planets in the HZ will be crucial for understanding planetary cycles, similar to Earth’s water cycle.

There are significant degeneracies in the retrievals from all modern Earth-reflectance observations. In the absence of clouds, the planetary radius shows significant degeneracies with surfaces that lack characteristic spec-

tral features in the VIS and NIR, such as the ocean and sand. We find that the combination of degeneracies significantly underestimates ocean coverage across all models, and often significantly overestimates sand coverage. Additional polarimetric phase curves may enable better-informed priors on ocean coverage in retrievals by detecting ocean glint (T. D. Robinson et al. 2010; S. R. Vaughan et al. 2023; N. B. Cowan et al. 2025). The planet-star contrast ratio scales as $F_p/F_s \propto R_p^2 A_g(\lambda)$, so two scenarios are possible: either a small planet with a bright surface or a large planet with a dim surface. That is, an underestimation of R_p can be compensated by adjusting the surface composition; increasing f_{sand} while decreasing f_{ocean} can normalize the overall flux to the decrease in radius. We find that the retrieval underestimates R_p for all spectral models, except the 100% cloud-coverage model. The degeneracies present on R_p are analogous to studies of brown dwarf spectra, which find the radius difficult to constrain within expected physical limits (B. Burningham et al. 2021; C. E. Hood et al. 2023; D. Kitzmann et al. 2020; A. Lueber et al. 2022; W. Ceva et al. 2025).

Retrievals from VIS and NIR observations of the planet alone, for a single 100-hour visit, can not yet identify land fraction coverage sufficiently to break the degeneracy between surface albedo and planetary radius without *a priori* information about R_p . An opaque cloud deck can also produce a similar effect: F_p/F_s increases with f_{cloud} and is degenerate with surface coverage. In the posterior distributions of all models, shown in Figs. 14-18, these degeneracies can clearly be seen. Despite the degeneracies between surface components, we find that f_{forest} was the most consistently detected material due to chlorophyll’s spectral signatures that are distinct from those of any other surface reflection included in our model. However, a single constrained biota-surface coverage detection is insufficient to support claims about potential life on the planet’s surface. Multiple surface materials could have identifiable false positive red-edge-like signals, such as iron oxide (S. R. Borges et al. 2024), cinnabar, and sulfur (N. Parenteau et al. 2026). Similar to how biosignature gases are sought for in combination to rule out false positives (L. Kaltenecker 2017; E. W. Schwieterman et al. 2018), surface biopigments need to be assessed in context (V. Meadows et al. 2022).

To identify specific surface coverage using retrievals currently requires *a priori* information about the planet. In addition, as shown in the retrieval using the model from G. Rocchetti et al. (2025) in Sec. 3.2.2, improper assumptions about the material used to model surface reflectivity can significantly bias the retrieved spectrum.

While work has begun on creating standard sets of spectra to use for exoplanet modeling (S. Hegde & L. Kaltenegger 2013; S. Hegde et al. 2015; J. T. O’Malley-James & L. Kaltenegger 2018a, 2019; G. Roccetti et al. 2024; L. F. Coelho et al. 2022, 2024; L. F. Coelho et al. 2025), working together to expand current databases with new measurements that cover wider wavelength ranges and determine a representative set of standard spectra is a critical next step for the community. Future work should also explore retrievals using a large, diverse set of surface spectra to determine whether current retrieval algorithms can distinguish surface signals in reflected-light observations across a wide range of surfaces, identify degeneracies, and disfavor false positives. This should also include further analysis into the effect spectral heterogeneity (Z. Burr et al. 2026) and surface configuration has on surface spectra retrievals. Other methods, including agnostic surface-retrieval methods that retrieve parametric surface albedos (F. Wang et al. 2022; J. Gomez Barrientos et al. 2023; A. G. Ulses et al. 2025; Z. Burr et al. 2026), will be significantly less biased by choices in lab data, but cannot determine constraints on surface fraction coverage. A combination of the two methods would likely be the most robust: first performing agnostic surface retrievals to extract key features in the planet’s reflection spectra, such as a red edge-like feature, and then using those features to inform the selection of lab-based spectroscopic retrieval datasets.

5. CONCLUSIONS

Reflected light from the surfaces of terrestrial exoplanets provides a unique opportunity to constrain the coverage of surface materials and biopigments. However, detailed studies assessing whether current HWO designs can retrieve such surface features in single-visit observations have not been available. Using five modern Earth spectral models at quadrature and complex noise modeling for the HWO Exploratory Analytic Case 5, we simulated single-visit HWO observations and performed

spectral retrievals with the open-source code POSEIDON to assess our ability to constrain both the surface and atmospheric compositions.

Our work suggests that state-of-the-art atmospheric retrieval algorithms currently used for exoplanet observations show promise in constraining the surface composition of reflected-light HWO observations. However, when *a priori* information about the planetary radius and surface is unavailable, we found that significant degeneracies complicate proper classification of the radius, surface pressure, surface composition, and cloud cover. We also found that bright clouds can enhance the detection of key atmospheric species but suppress surface spectral signals, complicating the detection of surface biopigments, such as the chlorophyll-induced red edge on modern Earth.

Our analysis shows that exploring degeneracies in VIS/NIR HWO observations and the biases inherent in current reflected-light retrievals will be critical priorities for mission design and data analysis. We find that it is critical to mature these techniques and develop concrete strategies for detecting surface features and breaking degeneracies before the first light of next-generation observatories.

ACKNOWLEDGMENTS

A.S.Z. would like to thank the support from the New York Space Grant. We would also like to thank Ryan MacDonald and Giulia Roccetti for helpful comments. This material is based upon work supported by the National Aeronautics and Space Administration under Grant No. 80NSSC24K0139 issued through the ROSES 2022: Astrophysics Decadal Survey Precursor Science program and through a NASA Cooperative Agreement awarded to the New York Space Grant Consortium. Any opinions, findings, conclusions or recommendations expressed in this material are those of the authors and do not necessarily reflect the views of NASA.

APPENDIX

A. COUNT RATES

Here we describe and review the components of the photon count rates that are used to compute the SNR in Eqn. 5. The count rate equations below are adapted from R. A. Brown (2005); C. C. Stark et al. (2014); D. Garrett et al. (2017); T. D. Robinson et al. (2016); J. Lustig-Yaeger et al. (2019), with the forms specifically following T. D. Robinson et al. (2016). The count rate from the planet is defined as

$$c_p = q(\lambda) \tau_{\text{core}}(\alpha, \lambda_0) \mathcal{T}(\lambda) \frac{\lambda}{hc} F_{p,\lambda}(d) \Delta\lambda A, \quad (\text{A1})$$

where $\frac{\lambda}{hc}F_{p,\lambda}(d)$ is the photon flux density of the planet at a distance d away, and $\Delta\lambda$ is the observing bandpass. For ease of reading, we hereafter shorten $q(\lambda)$, $\mathcal{T}(\lambda)$, and $\tau_{\text{core}}(\alpha, \lambda_0)$ to q , \mathcal{T} , and τ_{core} , respectively. Contamination from the stellar residual is given by

$$c_{\text{sr}} = Cq\tau_{\text{core}}\mathcal{T}\frac{\lambda}{hc}F_{s,\lambda}(d)\Delta\lambda A, \quad (\text{A2})$$

where C is the observatory's raw contrast. This is effectively the stellar count rate modified by the observatory's contrast.

The zodiacal light within coronagraph is computed as

$$c_z = Aq\tau_{\text{core}}\mathcal{T}\Omega\Delta\lambda\frac{\lambda}{hc}\frac{F_{\odot,\lambda}(1\text{ AU})}{F_{\odot,V}(1\text{ AU})}F_{0,V}10^{-0.4M_{z,V}} \quad (\text{A3})$$

where $F_{0,V} = 3.6 \times 10^{-8} \text{ Wm}^{-2} \mu\text{m}^{-1}$ is the standard zero-magnitude V-band specific flux density and $F_{\odot,V}$ is the solar flux density in V-band. Similarly, $F_{\odot,\lambda}$ is the wavelength-dependent solar flux density. The V-band surface brightness of the zodi in units of magnitudes per unit solid angle is given by $M_{z,V}$, where the median V-band brightness at a longitude of 135 degrees is 23 mag arcsec $^{-2}$ (C. C. Stark et al. 2014), which we adopt in our work. The photometric aperture area is Ω with units of arcsec $^{-2}$. Similar to how we computed τ_{core} in Sec. 2.4.1, we assume a circular photometric aperture with radius $\sqrt{2}/2 \lambda/D$, yielding a photometric aperture area of $\Omega = \pi/2 (\lambda/D)^2$. The exozodiacal dust count rate is similarly parameterized to the local zodiacal dust count rate, as

$$c_{\text{ez}} = Aq\tau_{\text{core}}\mathcal{T}\Omega\Delta\lambda\frac{\lambda}{hc}\left(\frac{1\text{AU}}{r}\right)^2\frac{F_{s,\lambda}(1\text{ AU})}{F_{s,V}(1\text{ AU})}\frac{F_{s,V}(1\text{ AU})}{F_{\odot,V}(1\text{ AU})}F_{0,V}N_{\text{ez}}10^{-0.4M_{\text{ez},V}}, \quad (\text{A4})$$

where r is the exoplanet's orbital distance. Similarly to Equation A3, $M_{\text{ez},V}$ is the V-band surface brightness of the exozodiacal disk in units of mag arcsec $^{-2}$ where N_{ez} is the number of exozodis in the disk. For our work, we assume 1 zodi ($N_{\text{ez}} = 1$) and an exozodiacal surface brightness of $M_{\text{ez},V} = 22$ mag arcsec $^{-2}$ for a solar twin (C. C. Stark et al. 2014).

From the specific detectors aboard the observatory, the count rate sourced from the dark current is defined by

$$c_{\text{DC}} = n_{\text{pix}}D_{e-}, \quad (\text{A5})$$

where n_{pix} is the number of pixels used inside the photometric aperture and D_{e-} is the dark current in electrons per pixel per unit time. We assume the spectrum is sampled at $\Delta N_{\text{pix}} = 3$ pixels per lenslet, where the diffraction limit at the minimum wavelength of the observing mode λ_{min} determines the lenslet diameter, $\theta_{\text{lens}} = \lambda_{\text{min}}/D/2$. Following T. D. Robinson et al. (2016) (see Eqn. A17), the number of pixels for the IFS is computed using $n_{\text{pix}} = 8\Delta N_{\text{pix}}\Omega/\pi\theta_{\text{lens}}^2$.

Similarly, the count rate due to the read noise (RN) is given as

$$c_{\text{RN}} = n_{\text{pix}}\frac{R_{e-}}{t_{\text{read}}} \quad (\text{A6})$$

where R_{e-} is the read noise in electrons per pixel and t_{read} is the time of each readout. Count rates from the clock-induced charge (CIC) are given by

$$c_{\text{CIC}} = n_{\text{pix}}\frac{R_c}{t_{\text{read}}}, \quad (\text{A7})$$

where R_c is the detector-specific CIC in electrons per pixel and assume $t_{\text{read}} = 1000$ s (The LUVUOIR Team 2019) for both the CIC and RN. Thermal noise contributions from the observatory are also included,

$$c_{\text{th}} = q\Omega\tau_{\text{core}}\mathcal{T}\frac{\lambda}{hc}\epsilon_{\text{sys}}B_{\lambda}(T_{\text{sys}})\Delta\lambda A, \quad (\text{A8})$$

where $B_{\lambda}(T_{\text{sys}})$ is the Planck blackbody function for a telescope of temperature T_{sys} and effective emissivity ϵ_{sys} , which is of order unity. We assume the observatory is kept at an ambient temperature of $T_{\text{sys}} = 270$ K.

We add a term into the SNR equation similar to [D. Garrett et al. \(2017\)](#) that accounts for variation in the residual stellar speckle

$$c_{\text{sp}} = c_{\text{sr}} f_{\text{pp}}, \quad (\text{A9})$$

where f_{pp} is a post-processing factor. The post-processing factor determines the stability of the PSF, such that $f_{\text{pp}} = 0.1$ corresponds to a 10-fold reduction in the stellar residual, which is the value we assume for our analysis. We note how c_{sp} is not scaled by the exposure time in Eqn. 5, setting the noise floor of our observations in the limit

$$\lim_{t_{\text{exp}} \rightarrow \infty} \text{SNR} = c_{\text{p}}/c_{\text{sp}}. \quad (\text{A10})$$

Thus, even for infinitely long exposures, we find that resolving the planetary signal remains dependent on the ability to reduce and stabilize the speckle residual PSF.

B. FIXED NOISE RETRIEVAL

To ensure single noise draws from simulating observations with Gaussian noise are not driving the retrieval results, it is often recommended to perform a suite of retrievals on numerous noise realizations. However, reflected light retrievals can take thousands of hours of compute time each, making this analysis unfeasible. As [Y. K. Feng et al. \(2018\)](#) noted, a compromise is to fix the data on the true flux values and add error bars to the data points scaled by the SNR. We performed a retrieval analysis of the $f_{\text{cloud}} = 0.5$ model described in Sec. 2.1 while fixing the data points to the true flux values. The results of this retrieval are shown in Fig. 12. We find the degeneracies present in this fixed noise model are consistent with those discussed in Sec. 3.1.2. There is a significant degeneracy between R_p and f_{cloud} , where the reported radius is significantly underestimated with an overestimation of cloud coverage.

C. FACTOR-OF-2 RADIUS PRIOR RETRIEVAL

We ran a retrieval with a tighter uniform prior on R_p of $\mathcal{U}(0.5, 2.0)$ to assess where the constrained parameter space influences the retrieval results. We performed this analysis using the $f_{\text{cloud}} = 0.5$, Gaussian-scattered spectral model described in Sec. 2.1. The retrieval results for the factor-of-2 radius prior are shown in Fig. 13. The tighter uniform radius prior does not provide any significant improvement in the performance of the retrieval. We find the shape of the posterior distribution of R_p is similar to the retrievals in Sec. 3.1.2 which uses the conservative $\mathcal{U}(0.1, 10)$ radius prior. This is likely due to the fact that the posterior distribution of R_p in Fig. 8 is fully constrained within the range of 0.5 to 2.0 R_{\oplus} . Thus, further *a priori* information on the radius distribution is needed to provide ample constraints. Future work should investigate performing retrievals coupled with photometric observations of the planet at different points in its orbit to determine if non-uniform constraints on the radius can be placed. This would also require an analysis of the potential biases this introduces into constraining other parameters in the retrieval algorithm, which is outside the scope of this work.

D. RETRIEVAL CORNER PLOTS

Figs. 14-18 show the full corner plots for the retrievals. The posterior median and 1- σ limits are shown above the marginalized distribution for each parameter. Where possible, the reference values used to create the spectra are included in teal lines in the posteriors.

REFERENCES

- Anderson, G. P., Clough, S. A., Kneizys, F. X., Chetwynd, J. H., & Shettle, E. P. 1986, AFGL atmospheric constituent profiles (0.120km),
- Barstow, J. K., & Heng, K. 2020, *SSRv*, 216, 82, doi: [10.1007/s11214-020-00666-x](https://doi.org/10.1007/s11214-020-00666-x)
- Batalha, N. E., Marley, M. S., Lewis, N. K., & Fortney, J. J. 2019, *The Astrophysical Journal*, 878, 70, doi: [10.3847/1538-4357/ab1b51](https://doi.org/10.3847/1538-4357/ab1b51)
- Beatty, T. G., Welbanks, L., Schlawin, E., et al. 2024, *ApJL*, 970, L10, doi: [10.3847/2041-8213/ad55e9](https://doi.org/10.3847/2041-8213/ad55e9)
- Bell, T. J., Welbanks, L., Schlawin, E., et al. 2023, *Nature*, 623, 709, doi: [10.1038/s41586-023-06687-0](https://doi.org/10.1038/s41586-023-06687-0)
- Benneke, B., Roy, P.-A., Coulombe, L.-P., et al. 2024, arXiv e-prints, arXiv:2403.03325, doi: [10.48550/arXiv.2403.03325](https://doi.org/10.48550/arXiv.2403.03325)

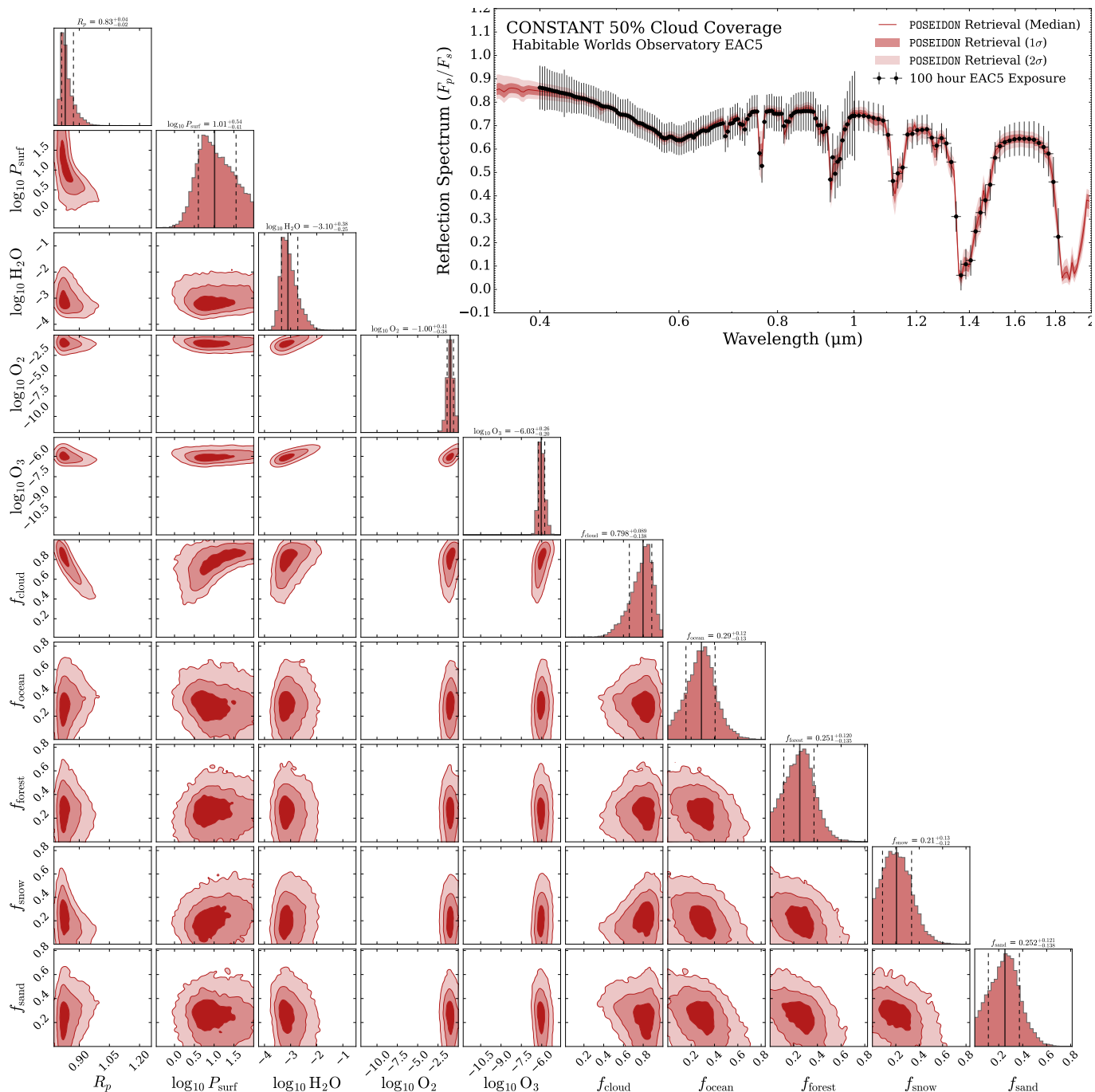


Figure 12. Retrieval results for the self-consistent POSEIDON spectra with 50% cloud coverage with fixed data on the true flux values. The posterior distributions for selected parameters are shown on the left-hand side, along with the median-retrieved spectra and simulated data in the top-right panel. The marginalized median and 1σ intervals for each parameter are labeled above the distributions and are shown in the black solid and dashed lines, respectively.

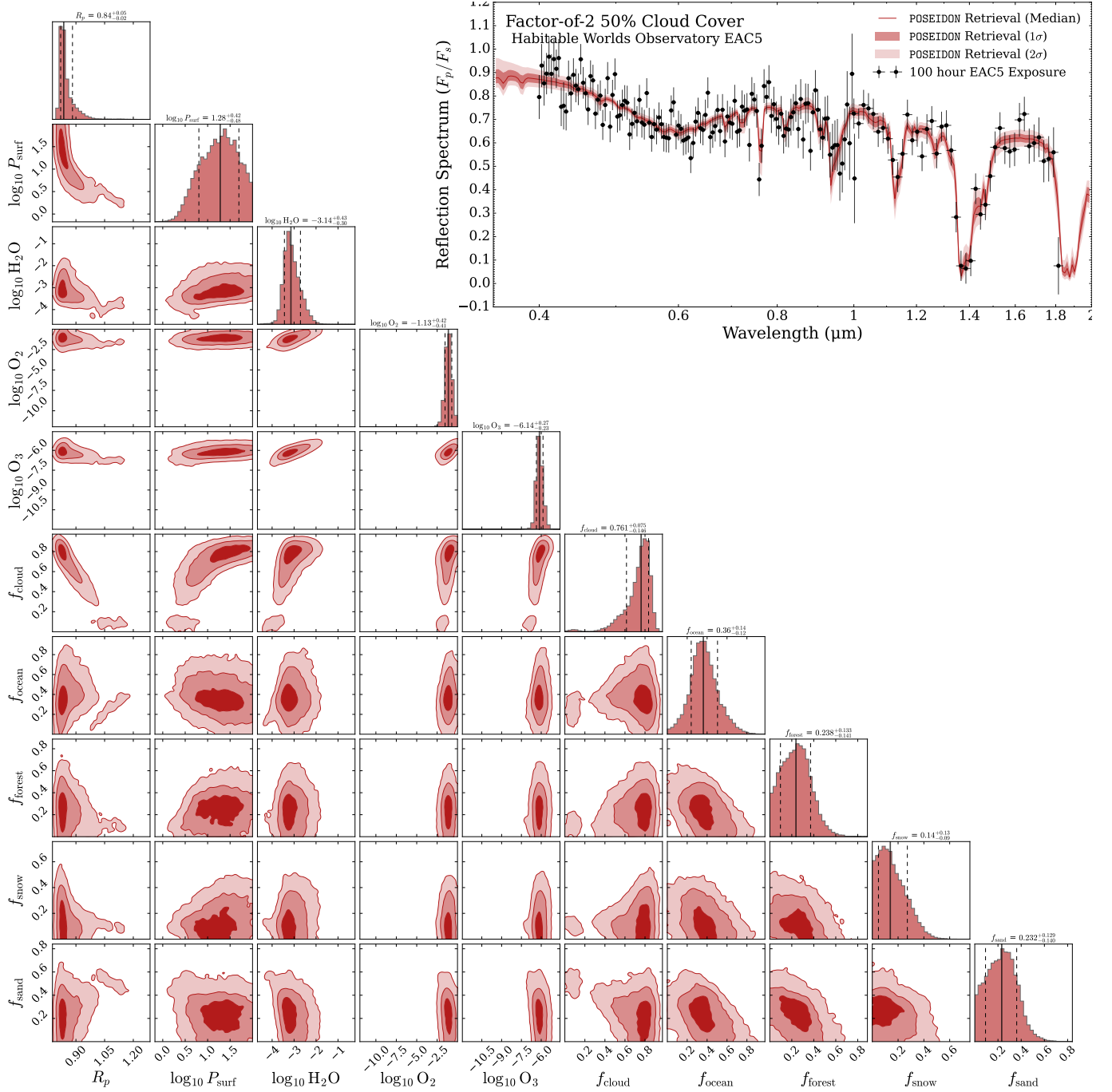


Figure 13. Retrieval results for the self-consistent POSEIDON spectra with 50% cloud coverage and tighter radius prior of $\mathcal{U}(0.5, 2.0)$. The posterior distributions for selected parameters are shown on the left-hand side, along with the median-retrieved spectra and simulated data in the top-right panel. The marginalized median and 1σ intervals for each parameter are labeled above the distributions and are shown in the black solid and dashed lines, respectively.

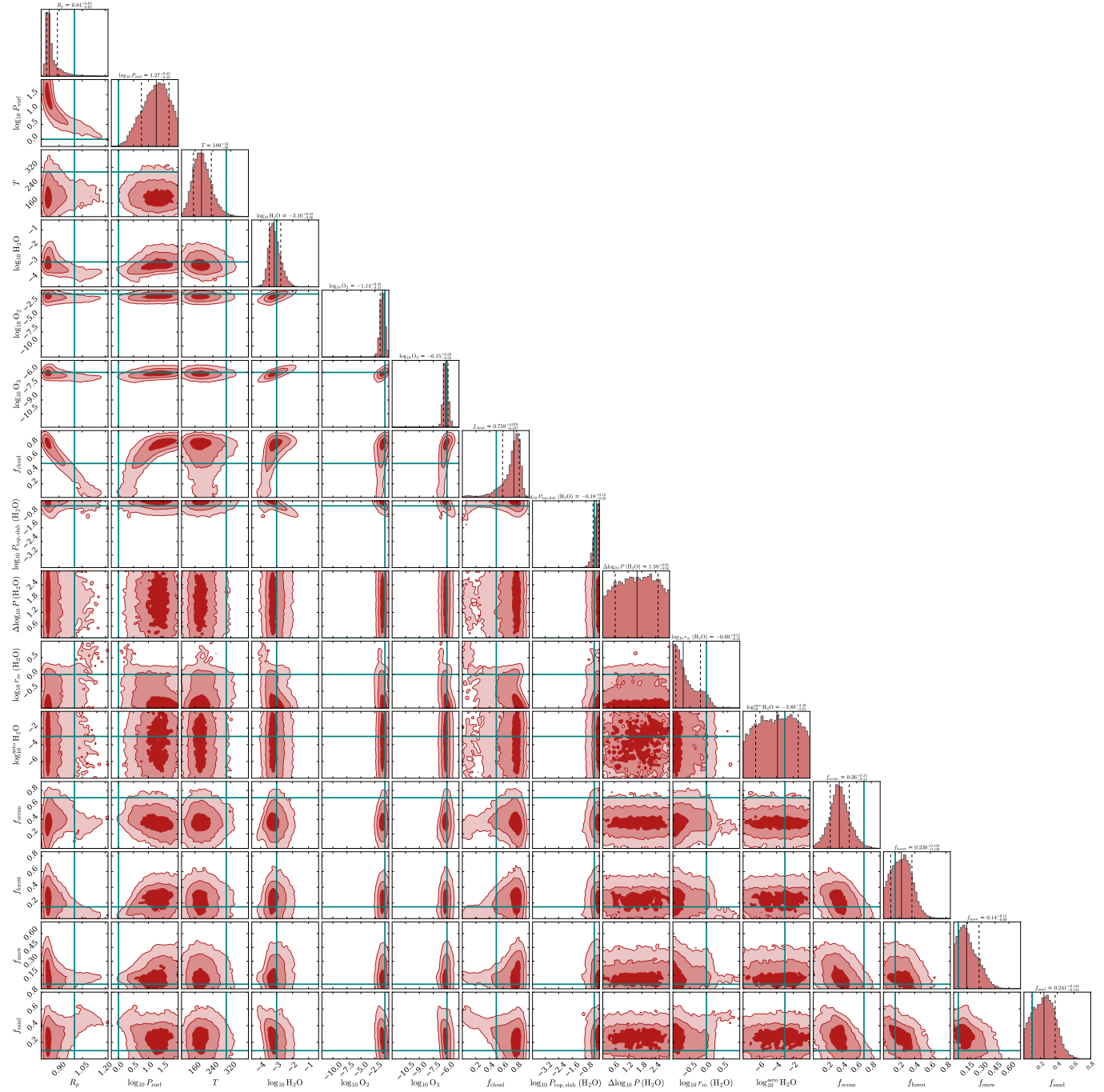


Figure 15. Full corner plot of the 50% cloud coverage, self-consistent POSEIDON model retrieval.

Burr, Z., Damiano, M., Kofman, V., Hu, R., & Villanueva, G. L. 2026, arXiv e-prints, arXiv:2603.20033.
<https://arxiv.org/abs/2603.20033>

Ceva, W., Matthews, E. C., Rickman, E. L., et al. 2025, A&A, 701, A78, doi: 10.1051/0004-6361/202555310

Christiansen, J. L., McElroy, D. L., Harbut, M., et al. 2025, The NASA Exoplanet Archive and Exoplanet Follow-up Observing Program: Data, Tools, and Usage, arXiv, doi: 10.48550/arXiv.2506.03299

Coelho, L. F., Kaltenecker, L., Philpot, W., et al. 2025, ApJL, 994, L2, doi: 10.3847/2041-8213/ae129a

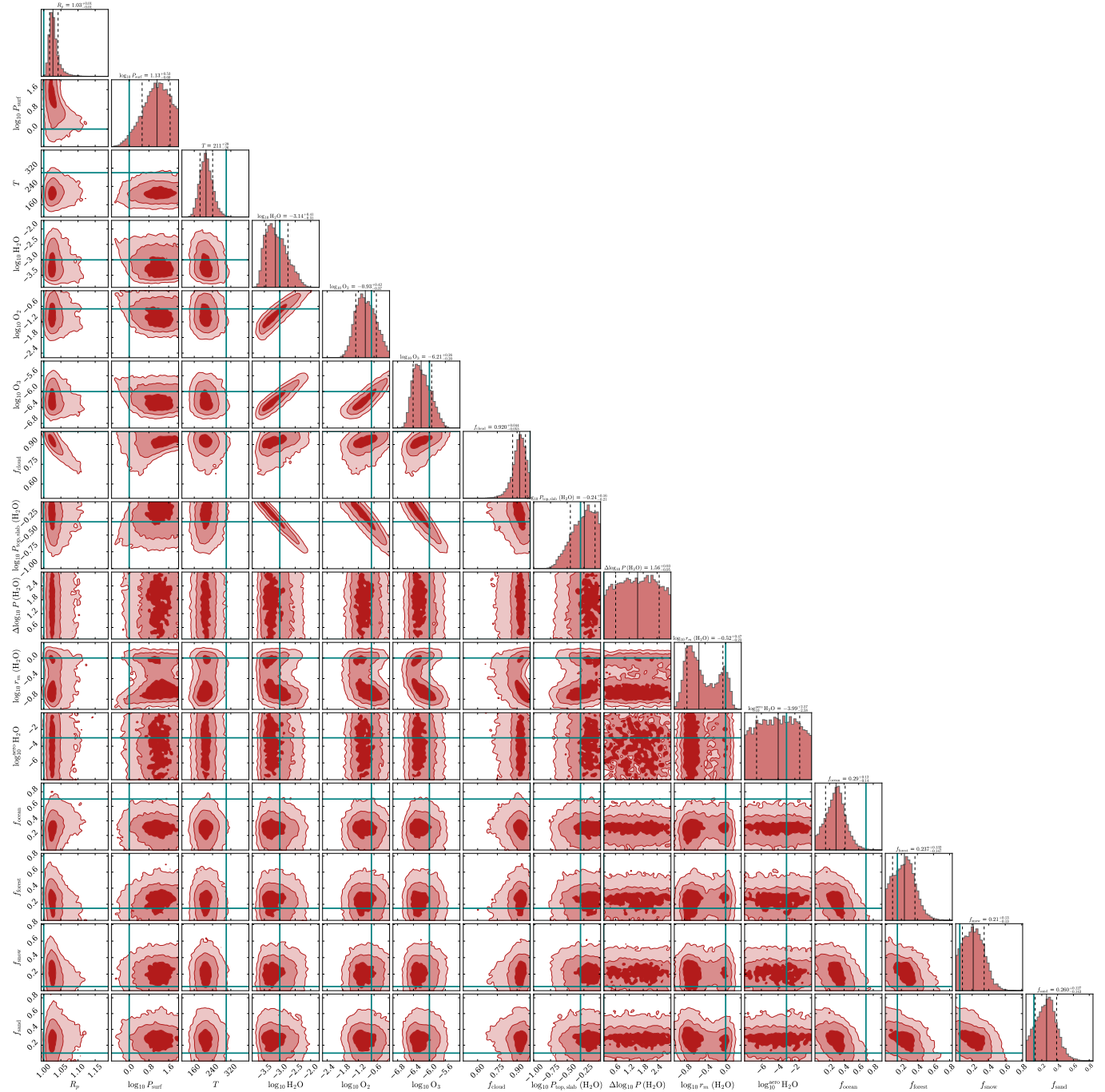


Figure 16. Full corner plot of the 100% cloud coverage, self-consistent POSEIDON model retrieval.

Coelho, L. F., Kaltenecker, L., Zinder, S., et al. 2024,
 Monthly Notices of the Royal Astronomical Society, 530,
 1363, doi: [10.1093/mnras/stae601](https://doi.org/10.1093/mnras/stae601)

Coelho, L. F., Madden, J., Kaltenecker, L., et al. 2022,
 Astrobiology, 22, 313, doi: [10.1089/ast.2021.0008](https://doi.org/10.1089/ast.2021.0008)

Coulombe, L.-P., Benneke, B., Challener, R., et al. 2023,
 Nature, 620, 292, doi: [10.1038/s41586-023-06230-1](https://doi.org/10.1038/s41586-023-06230-1)

Cowan, N. B., Lustig-Yaeger, J., Hu, R., Mayorga, L. C., &
 Robinson, T. D. 2025, arXiv e-prints, arXiv:2507.03071,
 doi: [10.48550/arXiv.2507.03071](https://doi.org/10.48550/arXiv.2507.03071)

Damiano, M., & Hu, R. 2022, AJ, 163, 299,
 doi: [10.3847/1538-3881/ac6b97](https://doi.org/10.3847/1538-3881/ac6b97)

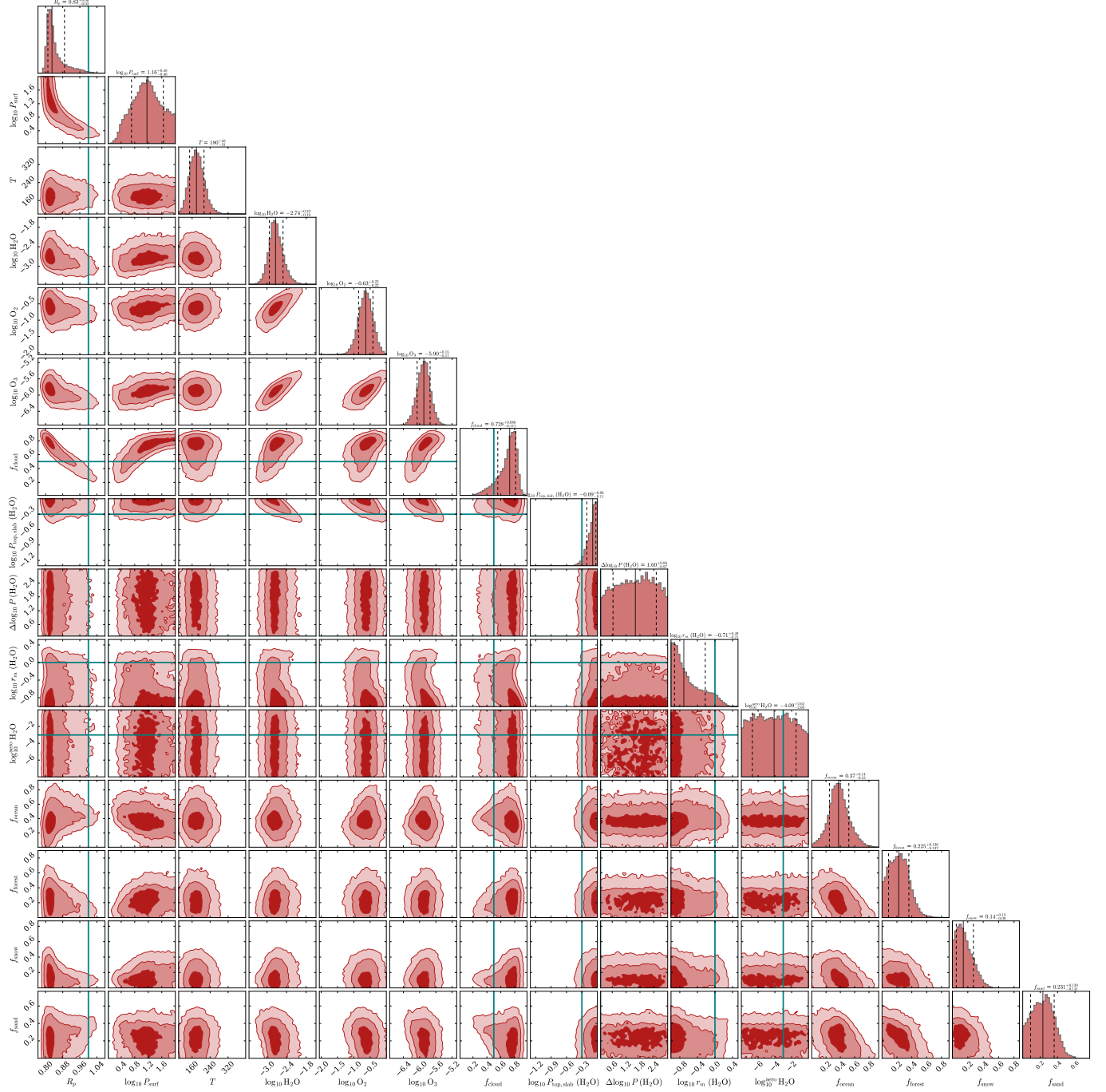


Figure 17. Full corner plot of the MODIS surface and L. Kaltenegger et al. (2020a) atmospheric model retrieval.

Delacroix, C., Savransky, D., Garrett, D., Lowrance, P., & Morgan, R. 2016, in Society of Photo-Optical Instrumentation Engineers (SPIE) Conference Series, Vol. 9911, Modeling, Systems Engineering, and Project Management for Astronomy VI, ed. G. Z. Angeli & P. Dierickx, 991119, doi: [10.1117/12.2233913](https://doi.org/10.1117/12.2233913)

Dittmann, A. 2024, The Open Journal of Astrophysics, 7, 79, doi: [10.33232/001c.123872](https://doi.org/10.33232/001c.123872)

Dyrek, A., Min, M., Decin, L., et al. 2024, Nature, 625, 51, doi: [10.1038/s41586-023-06849-0](https://doi.org/10.1038/s41586-023-06849-0)

Espinoza, N., Allen, N. H., Glidden, A., et al. 2025, ApJL, 990, L52, doi: [10.3847/2041-8213/adf42e](https://doi.org/10.3847/2041-8213/adf42e)

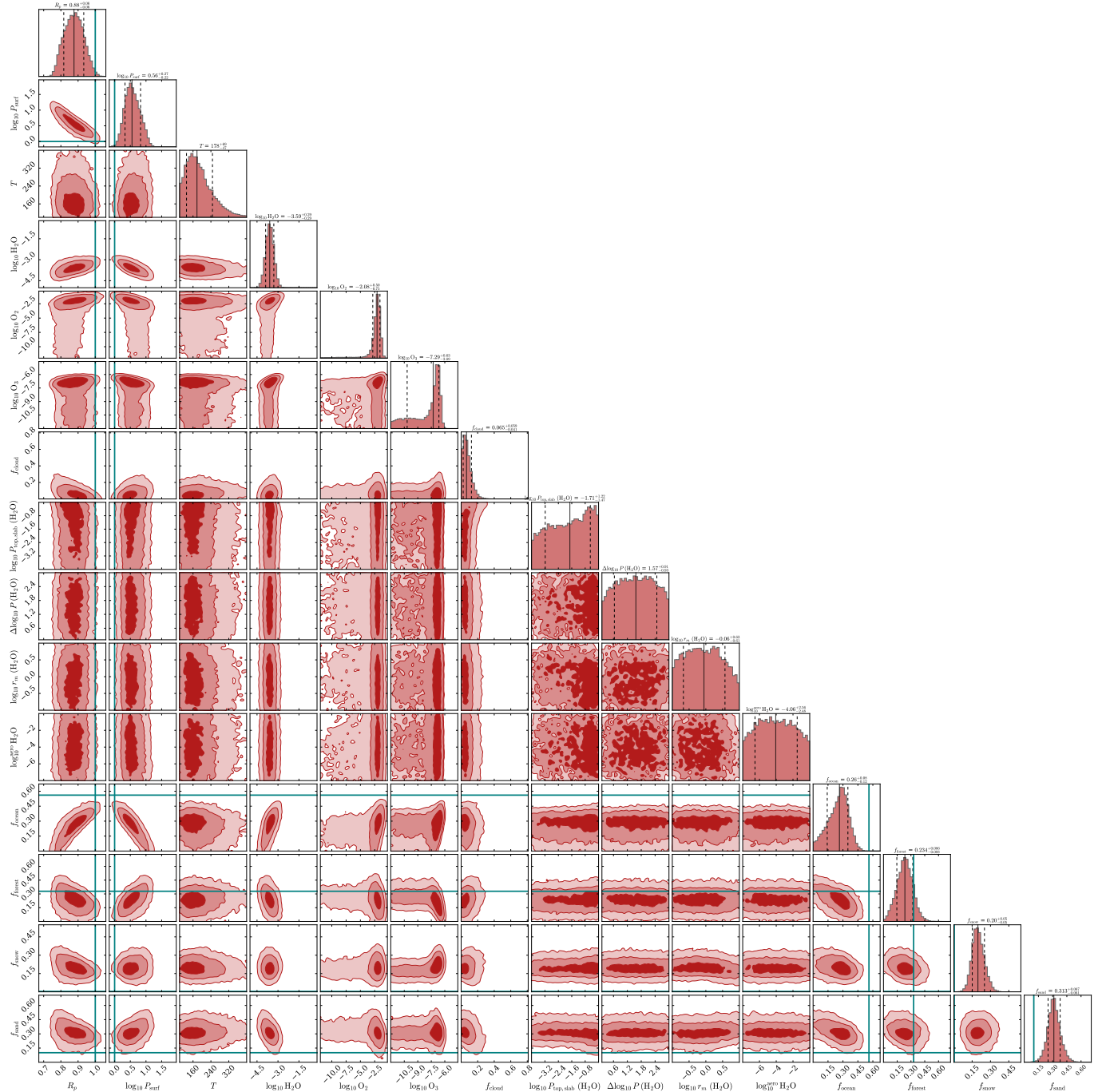


Figure 18. Full corner plot of the [G. Rocetti et al. \(2025\)](#) model retrieval.

Feinberg, L., Ziemer, J., Ansdell, M., et al. 2024, in *Space Telescopes and Instrumentation 2024: Optical, Infrared, and Millimeter Wave*, ed. L. E. Coyle, S. Matsuura, & M. D. Perrin, Vol. 13092, International Society for Optics and Photonics (SPIE), 130921N, doi: [10.1117/12.3018328](https://doi.org/10.1117/12.3018328)

Feinberg, L. D., Sitarski, B. N., McElwain, M. W., et al. 2026, arXiv e-prints, arXiv:2601.11803, doi: [10.48550/arXiv.2601.11803](https://doi.org/10.48550/arXiv.2601.11803)

Feng, Y. K., Robinson, T. D., Fortney, J. J., et al. 2018, *AJ*, 155, 200, doi: [10.3847/1538-3881/aab95c](https://doi.org/10.3847/1538-3881/aab95c)

Feroz, F., Hobson, M. P., & Bridges, M. 2009, *MNRAS*, 398, 1601, doi: [10.1111/j.1365-2966.2009.14548.x](https://doi.org/10.1111/j.1365-2966.2009.14548.x)

Fortney, J. J., Lupu, R. E., Morley, C. V., Freedman, R. S., & Hood, C. 2019, *ApJL*, 880, L16, doi: [10.3847/2041-8213/ab2a10](https://doi.org/10.3847/2041-8213/ab2a10)

- Fortune, M., Gibson, N. P., Diamond-Lowe, H., et al. 2025, *A&A*, 701, A25, doi: [10.1051/0004-6361/202554198](https://doi.org/10.1051/0004-6361/202554198)
- Friedl, M., & Sulla-Menashe, D. 2022, MODIS/Terra+Aqua Land Cover Type Yearly L3 Global 0.05Deg CMG V061, NASA Land Processes Distributed Active Archive Center, doi: [10.5067/MODIS/MCD12C1.061](https://doi.org/10.5067/MODIS/MCD12C1.061)
- Fulton, B. J., Petigura, E. A., Howard, A. W., et al. 2017, *AJ*, 154, 109, doi: [10.3847/1538-3881/aa80eb](https://doi.org/10.3847/1538-3881/aa80eb)
- Garrett, D., Savransky, D., & Macintosh, B. 2017, *AJ*, 154, 47, doi: [10.3847/1538-3881/aa78f6](https://doi.org/10.3847/1538-3881/aa78f6)
- Gaudi, B. S., Seager, S., Mennesson, B., et al. 2020, The Habitable Exoplanet Observatory (HabEx) Mission Concept Study Final Report, doi: [10.48550/arXiv.2001.06683](https://doi.org/10.48550/arXiv.2001.06683)
- Glidden, A., Ranjan, S., Seager, S., et al. 2025, *ApJL*, 990, L53, doi: [10.3847/2041-8213/adf62e](https://doi.org/10.3847/2041-8213/adf62e)
- Gomez Barrientos, J., MacDonald, R. J., Lewis, N. K., & Kaltenegger, L. 2023, *The Astrophysical Journal*, 946, 96, doi: [10.3847/1538-4357/acaf59](https://doi.org/10.3847/1538-4357/acaf59)
- Goodis Gordon, K. E., Karalidi, T., Bott, K. M., et al. 2024, Polarized Signatures of the Earth Through Time: An Outlook for the Habitable Worlds Observatory, doi: [10.48550/arXiv.2410.02194](https://doi.org/10.48550/arXiv.2410.02194)
- Gordon, I. E., Rothman, L. S., Hill, C., et al. 2017, *JQSRT*, 203, 3, doi: [10.1016/j.jqsrt.2017.06.038](https://doi.org/10.1016/j.jqsrt.2017.06.038)
- Gordon, I. E., Rothman, L. S., Hargreaves, R. J., et al. 2022, *Journal of Quantitative Spectroscopy and Radiative Transfer*, 277, 107949, doi: [10.1016/j.jqsrt.2021.107949](https://doi.org/10.1016/j.jqsrt.2021.107949)
- Grant, D., Lewis, N. K., Wakeford, H. R., et al. 2023, *ApJL*, 956, L32, doi: [10.3847/2041-8213/acfc3b10.3847/2041-8213/acfdab](https://doi.org/10.3847/2041-8213/acfc3b10.3847/2041-8213/acfdab)
- Grenfell, T. C., Warren, S. G., & Mullen, P. C. 1994, *Journal of Geophysical Research: Atmospheres*, 99, 18669, doi: [10.1029/94JD01484](https://doi.org/10.1029/94JD01484)
- Hale, G. M., & Querry, M. R. 1973, *ApOpt*, 12, 555, doi: [10.1364/AO.12.000555](https://doi.org/10.1364/AO.12.000555)
- Hapke, B. 2012, Theory of Reflectance and Emittance Spectroscopy, doi: [10.1017/CBO9781139025683](https://doi.org/10.1017/CBO9781139025683)
- Harrison, E. F., Minnis, P., Barkstrom, B., et al. 1990, *Journal of Geophysical Research: Atmospheres*, 95, 18687
- Hartmann, D. L., Ockert-Bell, M. E., & Michelsen, M. L. 1992, *Journal of Climate*, 5, 1281, doi: [10.1175/1520-0442\(1992\)005\(1281:TEOCTO\)2.0.CO;2](https://doi.org/10.1175/1520-0442(1992)005(1281:TEOCTO)2.0.CO;2)
- Hegde, S., & Kaltenegger, L. 2013, *Astrobiology*, 13, 47, doi: [10.1089/ast.2012.0849](https://doi.org/10.1089/ast.2012.0849)
- Hegde, S., Paulino-Lima, I. G., Kent, R., Kaltenegger, L., & Rothschild, L. 2015, *Proceedings of the National Academy of Science*, 112, 3886, doi: [10.1073/pnas.1421237112](https://doi.org/10.1073/pnas.1421237112)
- Heney, L. G., & Greenstein, J. L. 1941, *ApJ*, 93, 70, doi: [10.1086/144246](https://doi.org/10.1086/144246)
- Hersbach, H., Bell, B., Berrisford, P., et al. 2020, *Quarterly Journal of the Royal Meteorological Society*, 146, 1999, doi: [10.1002/qj.3803](https://doi.org/10.1002/qj.3803)
- Hood, C. E., Fortney, J. J., Line, M. R., & Faherty, J. K. 2023, *ApJ*, 953, 170, doi: [10.3847/1538-4357/ace32e](https://doi.org/10.3847/1538-4357/ace32e)
- Inglis, J., Batalha, N. E., Lewis, N. K., et al. 2024, *ApJL*, 973, L41, doi: [10.3847/2041-8213/ad725e](https://doi.org/10.3847/2041-8213/ad725e)
- Jennewein, J. S., Hively, W., Lamb, B. T., et al. 2024, *Precision Agriculture*, 25, 2165, doi: [10.1007/s11119-024-10159-4](https://doi.org/10.1007/s11119-024-10159-4)
- Kaltenegger, L. 2017, *Annual Review of Astronomy and Astrophysics*, 55, 433, doi: [10.1146/annurev-astro-082214-122238](https://doi.org/10.1146/annurev-astro-082214-122238)
- Kaltenegger, L., Lin, Z., & Madden, J. 2020a, *The Astrophysical Journal*, 892, L17, doi: [10.3847/2041-8213/ab789f](https://doi.org/10.3847/2041-8213/ab789f)
- Kaltenegger, L., Lin, Z., & Rugheimer, S. 2020b, *The Astrophysical Journal*, 904, 10, doi: [10.3847/1538-4357/abb9b2](https://doi.org/10.3847/1538-4357/abb9b2)
- Kaltenegger, L., & Traub, W. A. 2009, *ApJ*, 698, 519, doi: [10.1088/0004-637X/698/1/519](https://doi.org/10.1088/0004-637X/698/1/519)
- Kaltenegger, L., Traub, W. A., & Jucks, K. W. 2007, *The Astrophysical Journal*, 658, 598, doi: [10.1086/510996](https://doi.org/10.1086/510996)
- Karman, T., Gordon, I. E., van der Avoird, A., et al. 2019, *Icarus*, 328, 160, doi: [10.1016/j.icarus.2019.02.034](https://doi.org/10.1016/j.icarus.2019.02.034)
- Kitzmann, D., Heng, K., Oreshenko, M., et al. 2020, *ApJ*, 890, 174, doi: [10.3847/1538-4357/ab6d71](https://doi.org/10.3847/1538-4357/ab6d71)
- Kokaly, R. F., Clark, R. N., Swayze, G. A., et al. 2017, USGS Spectral Library Version 7, Tech. Rep. 1035, U.S. Geological Survey, doi: [10.3133/ds1035](https://doi.org/10.3133/ds1035)
- Kopparapu, R. K., Hébrard, E., Belikov, R., et al. 2018, *The Astrophysical Journal*, 856, 122, doi: [10.3847/1538-4357/aab205](https://doi.org/10.3847/1538-4357/aab205)
- Lammer, H., Lichtenegger, H. I. M., Kulikov, Y. N., et al. 2007, *Astrobiology*, 7, 185, doi: [10.1089/ast.2006.0128](https://doi.org/10.1089/ast.2006.0128)
- Lin, Z., MacDonald, R. J., Kaltenegger, L., & Wilson, D. J. 2021, *MNRAS*, 505, 3562, doi: [10.1093/mnras/stab1486](https://doi.org/10.1093/mnras/stab1486)
- Lueber, A., Kitzmann, D., Bowler, B. P., Burgasser, A. J., & Heng, K. 2022, *ApJ*, 930, 136, doi: [10.3847/1538-4357/ac63b9](https://doi.org/10.3847/1538-4357/ac63b9)
- Lustig-Yaeger, J., Robinson, T., & Arney, G. 2019, *The Journal of Open Source Software*, 4, 1387, doi: [10.21105/joss.01387](https://doi.org/10.21105/joss.01387)
- MacDonald, R. J. 2023, *The Journal of Open Source Software*, 8, 4873, doi: [10.21105/joss.04873](https://doi.org/10.21105/joss.04873)
- MacDonald, R. J., & Batalha, N. E. 2023, *Research Notes of the American Astronomical Society*, 7, 54, doi: [10.3847/2515-5172/acc46a](https://doi.org/10.3847/2515-5172/acc46a)

- MacDonald, R. J., & Lewis, N. K. 2022, *The Astrophysical Journal*, 929, 20, doi: [10.3847/1538-4357/ac47fe](https://doi.org/10.3847/1538-4357/ac47fe)
- MacDonald, R. J., & Madhusudhan, N. 2017, *Monthly Notices of the Royal Astronomical Society*, 469, 1979, doi: [10.1093/mnras/stx804](https://doi.org/10.1093/mnras/stx804)
- Madden, J., & Kaltenegger, L. 2020a, *Monthly Notices of the Royal Astronomical Society*, 495, 1, doi: [10.1093/mnras/staa387](https://doi.org/10.1093/mnras/staa387)
- Madden, J., & Kaltenegger, L. 2020b, *The Astrophysical Journal Letters*, 898, L42, doi: [10.3847/2041-8213/aba535](https://doi.org/10.3847/2041-8213/aba535)
- Madhusudhan, N. 2018, in *Handbook of Exoplanets*, ed. H. J. Deeg & J. A. Belmonte, 104, doi: [10.1007/978-3-319-55333-7_104](https://doi.org/10.1007/978-3-319-55333-7_104)
- Mamajek, E., & Stapelfeldt, K. 2024, arXiv e-prints, arXiv:2402.12414, doi: [10.48550/arXiv.2402.12414](https://doi.org/10.48550/arXiv.2402.12414)
- Mayer, B. 2009, in *European Physical Journal Web of Conferences*, Vol. 1, European Physical Journal Web of Conferences (EDP), 75, doi: [10.1140/epjconf/e2009-00912-1](https://doi.org/10.1140/epjconf/e2009-00912-1)
- Mayer, B., Hoch, S. W., & Whiteman, C. D. 2010, *Atmospheric Chemistry & Physics*, 10, 8685, doi: [10.5194/acp-10-8685-2010](https://doi.org/10.5194/acp-10-8685-2010)
- Meadows, V., Graham, H., Abrahamsson, V., et al. 2022, arXiv e-prints, arXiv:2210.14293, doi: [10.48550/arXiv.2210.14293](https://doi.org/10.48550/arXiv.2210.14293)
- Meerdink, S. K., Hook, S. J., Roberts, D. A., & Abbott, E. A. 2019, *Remote Sensing of Environment*, 230, 111196, doi: [10.1016/j.rse.2019.05.015](https://doi.org/10.1016/j.rse.2019.05.015)
- Mie, G. 1908, *Annalen der Physik*, 330, 377, doi: [10.1002/andp.19083300302](https://doi.org/10.1002/andp.19083300302)
- Mullens, E., & Lewis, N. K. 2025, *ApJL*, 988, L43, doi: [10.3847/2041-8213/ade885](https://doi.org/10.3847/2041-8213/ade885)
- Mullens, E., Lewis, N. K., & MacDonald, R. J. 2024, *ApJ*, 977, 105, doi: [10.3847/1538-4357/ad8575](https://doi.org/10.3847/1538-4357/ad8575)
- Mullens, E., MacDonald, R. J., Gemma, M. E., et al. 2026, Submitted, PSJ
- National Academies of Sciences, and Medicine, E. 2021, *Pathways to Discovery in Astronomy and Astrophysics for the 2020s*, doi: [10.17226/26141](https://doi.org/10.17226/26141)
- Neil, A. R., & Rogers, L. A. 2020, *ApJ*, 891, 12, doi: [10.3847/1538-4357/ab6a92](https://doi.org/10.3847/1538-4357/ab6a92)
- O'Malley-James, J. T., & Kaltenegger, L. 2018a, *Monthly Notices of the Royal Astronomical Society*, 481, 2487, doi: [10.1093/mnras/sty2411](https://doi.org/10.1093/mnras/sty2411)
- O'Malley-James, J. T., & Kaltenegger, L. 2018b, *Astrobiology*, 18, 1123, doi: [10.1089/ast.2017.1798](https://doi.org/10.1089/ast.2017.1798)
- O'Malley-James, J. T., & Kaltenegger, L. 2019, *The Astrophysical Journal*, 879, L20, doi: [10.3847/2041-8213/ab2769](https://doi.org/10.3847/2041-8213/ab2769)
- Parenteau, N., Ulses, A. G., Metz, C., et al. 2026, arXiv e-prints, arXiv:2601.08883, doi: [10.48550/arXiv.2601.08883](https://doi.org/10.48550/arXiv.2601.08883)
- Peacock, S., Wilson, D. J., Richey-Yowell, T., et al. 2025, *AJ*, 170, 293, doi: [10.3847/1538-3881/ae0a2f](https://doi.org/10.3847/1538-3881/ae0a2f)
- Por, E. H., Haffert, S. Y., Radhakrishnan, V. M., et al. 2018, in *Society of Photo-Optical Instrumentation Engineers (SPIE) Conference Series*, Vol. 10703, Adaptive Optics Systems VI, ed. L. M. Close, L. Schreiber, & D. Schmidt, 1070342, doi: [10.1117/12.2314407](https://doi.org/10.1117/12.2314407)
- Prahl, S. 2024, miepython: Pure python calculation of Mie scattering, 2.5.5 Zenodo, doi: [10.5281/zenodo.14257432](https://doi.org/10.5281/zenodo.14257432)
- Radica, M., Piaulet-Ghorayeb, C., Taylor, J., et al. 2025, *ApJL*, 979, L5, doi: [10.3847/2041-8213/ada381](https://doi.org/10.3847/2041-8213/ada381)
- Ramanathan, V., Cess, R. D., Harrison, E. F., et al. 1989, *Science*, 243, 57, doi: [10.1126/science.243.4887.57](https://doi.org/10.1126/science.243.4887.57)
- Rauer, H., Aerts, C., Cabrera, J., et al. 2025, *Experimental Astronomy*, 59, 26, doi: [10.1007/s10686-025-09985-9](https://doi.org/10.1007/s10686-025-09985-9)
- Robinson, T. D. 2025, *Inferring and Interpreting the Visual Geometric Albedo and Phase Function of Earth*, arXiv, doi: [10.48550/arXiv.2507.22258](https://doi.org/10.48550/arXiv.2507.22258)
- Robinson, T. D., Meadows, V. S., & Crisp, D. 2010, *ApJL*, 721, L67, doi: [10.1088/2041-8205/721/1/L67](https://doi.org/10.1088/2041-8205/721/1/L67)
- Robinson, T. D., Stapelfeldt, K. R., & Marley, M. S. 2016, *Publications of the Astronomical Society of the Pacific*, 128, 025003, doi: [10.1088/1538-3873/128/960/025003](https://doi.org/10.1088/1538-3873/128/960/025003)
- Robinson, T. D., Meadows, V. S., Crisp, D., et al. 2011, *Astrobiology*, 11, 393, doi: [10.1089/ast.2011.0642](https://doi.org/10.1089/ast.2011.0642)
- Rocchetti, G., Bugliaro, L., Götde, F., et al. 2024, *Atmospheric Measurement Techniques*, 17, 6025, doi: [10.5194/amt-17-6025-2024](https://doi.org/10.5194/amt-17-6025-2024)
- Rocchetti, G., Emde, C., Sterzik, M. F., et al. 2025, *Astronomy and Astrophysics*, 697, A170, doi: [10.1051/0004-6361/202554167](https://doi.org/10.1051/0004-6361/202554167)
- Rugheimer, S., Kaltenegger, L., Segura, A., Linsky, J., & Mohanty, S. 2015, *The Astrophysical Journal*, 809, 57, doi: [10.1088/0004-637X/809/1/57](https://doi.org/10.1088/0004-637X/809/1/57)
- Rugheimer, S., Kaltenegger, L., Zsom, A., Segura, A., & Sasselov, D. 2013, *Astrobiology*, 13, 251, doi: [10.1089/ast.2012.0888](https://doi.org/10.1089/ast.2012.0888)
- Rustamkulov, Z., Sing, D. K., Mukherjee, S., et al. 2023, *Nature*, 614, 659, doi: [10.1038/s41586-022-05677-y](https://doi.org/10.1038/s41586-022-05677-y)
- Sagan, C., Thompson, W. R., Carlson, R., Gurnett, D., & Hord, C. 1993, *Nature*, 365, 715, doi: [10.1038/365715a0](https://doi.org/10.1038/365715a0)
- Salomonson, V. V., Barnes, W. L., Maymon, P. W., Montgomery, H. E., & Ostrow, H. 1989, *IEEE Transactions on Geoscience and Remote Sensing*, 27, 145, doi: [10.1109/36.20292](https://doi.org/10.1109/36.20292)
- Salvador, A., & Robinson, T. D. 2025, arXiv e-prints, arXiv:2510.21973, doi: [10.48550/arXiv.2510.21973](https://doi.org/10.48550/arXiv.2510.21973)

- Savransky, D., & Garrett, D. 2016, *Journal of Astronomical Telescopes, Instruments, and Systems*, 2, 011006, doi: [10.1117/1.JATIS.2.1.011006](https://doi.org/10.1117/1.JATIS.2.1.011006)
- Scalo, J., Kaltenegger, L., Segura, A., et al. 2007, *Astrobiology*, 7, 85, doi: [10.1089/ast.2006.0125](https://doi.org/10.1089/ast.2006.0125)
- Schmidt, S. P., MacDonald, R. J., Tsai, S.-M., et al. 2025, *AJ*, 170, 298, doi: [10.3847/1538-3881/ae019a](https://doi.org/10.3847/1538-3881/ae019a)
- Schwieterman, E. W., & Leung, M. 2024, *Reviews in Mineralogy and Geochemistry*, 90, 465, doi: [10.2138/rmg.2024.90.13](https://doi.org/10.2138/rmg.2024.90.13)
- Schwieterman, E. W., Kiang, N. Y., Parenteau, M. N., et al. 2018, *Astrobiology*, 18, 663, doi: [10.1089/ast.2017.1729](https://doi.org/10.1089/ast.2017.1729)
- Seager, S., Turner, E. L., Schafer, J., & Ford, E. B. 2005, *Astrobiology*, 5, 372, doi: [10.1089/ast.2005.5.372](https://doi.org/10.1089/ast.2005.5.372)
- Serdychenko, A., Gorshchev, V., Weber, M., Chehade, W., & Burrows, J. P. 2014, *Atmospheric Measurement Techniques*, 7, 625, doi: [10.5194/amt-7-625-2014](https://doi.org/10.5194/amt-7-625-2014)
- Stark, C. C., Roberge, A., Mandell, A., & Robinson, T. D. 2014, *The Astrophysical Journal*, 795, 122, doi: [10.1088/0004-637X/795/2/122](https://doi.org/10.1088/0004-637X/795/2/122)
- Stubenrauch, C. J., Rossow, W. B., Kinne, S., et al. 2013, *Bulletin of the American Meteorological Society*, 94, 1031, doi: [10.1175/BAMS-D-12-00117.1](https://doi.org/10.1175/BAMS-D-12-00117.1)
- Taylor, J. 2022, *MNRAS*, 513, L20, doi: [10.1093/mnrasl/slac028](https://doi.org/10.1093/mnrasl/slac028)
- The LUVOIR Team. 2019, *The LUVOIR Mission Concept Study Final Report*, doi: [10.48550/arXiv.1912.06219](https://doi.org/10.48550/arXiv.1912.06219)
- Tinetti, G., Meadows, V. S., Crisp, D., et al. 2006, *Astrobiology*, 6, 34, doi: [10.1089/ast.2006.6.34](https://doi.org/10.1089/ast.2006.6.34)
- Tsai, S.-M., Lee, E. K. H., Powell, D., et al. 2023, *Nature*, 617, 483, doi: [10.1038/s41586-023-05902-2](https://doi.org/10.1038/s41586-023-05902-2)
- Tuchow, N. W., Harada, C. K., Mamajek, E. E., et al. 2025, *PASP*, 137, 104402, doi: [10.1088/1538-3873/ae0a81](https://doi.org/10.1088/1538-3873/ae0a81)
- Ulses, A. G., Krissansen-Totton, J., Robinson, T. D., et al. 2025, *The Astrophysical Journal*, 990, 48, doi: [10.3847/1538-4357/ade669](https://doi.org/10.3847/1538-4357/ade669)
- Vaughan, S. R., Gebhard, T. D., Bott, K., et al. 2023, *Monthly Notices of the Royal Astronomical Society*, 524, 5477, doi: [10.1093/mnras/stad2127](https://doi.org/10.1093/mnras/stad2127)
- Wakeford, H. R., & Sing, D. K. 2015, *A&A*, 573, A122, doi: [10.1051/0004-6361/201424207](https://doi.org/10.1051/0004-6361/201424207)
- Wang, F., Fujii, Y., & He, J. 2022, *The Astrophysical Journal*, 931, 48, doi: [10.3847/1538-4357/ac67e5](https://doi.org/10.3847/1538-4357/ac67e5)
- Wheatley, P. J., Louden, T., Bourrier, V., Ehrenreich, D., & Gillon, M. 2017, *MNRAS*, 465, L74, doi: [10.1093/mnrasl/slw192](https://doi.org/10.1093/mnrasl/slw192)
- Wielicki, B. A., Cess, R. D., King, M. D., Randall, D. A., & Harrison, E. F. 1995, *Bulletin of the American Meteorological Society*, 76, 2125, doi: [10.1175/1520-0477\(1995\)076\(2125:MTPERO\)2.0.CO;2](https://doi.org/10.1175/1520-0477(1995)076(2125:MTPERO)2.0.CO;2)
- Wilson, R. F., Barclay, T., Powell, B. P., et al. 2023, *ApJS*, 269, 5, doi: [10.3847/1538-4365/acf3df](https://doi.org/10.3847/1538-4365/acf3df)
- Wiscombe, W. J. 1979, *MIE scattering calculations, advances in technique and fast, vector-shaped computer codes*,
- Xue, Q., Bean, J. L., Zhang, M., et al. 2024, *ApJL*, 973, L8, doi: [10.3847/2041-8213/ad72e9](https://doi.org/10.3847/2041-8213/ad72e9)
- Zahnle, K. J., & Catling, D. C. 2017, *ApJ*, 843, 122, doi: [10.3847/1538-4357/aa7846](https://doi.org/10.3847/1538-4357/aa7846)